

Seismological Expression of the Iron Spin Crossover in Ferropericlase in the Earth's Lower Mantle

Grace E. Shephard*¹, Christine Houser², John W. Hernlund², Juan J. Valencia-Cardona³, Reidar G. Trønnes^{1,4}, Renata M. Wentzcovitch*^{5,6,7}

¹*Centre for Earth Evolution and Dynamics (CEED), Department of Geosciences, University of Oslo, Norway*

²*Earth-Life Science Institute, Tokyo Institute of Technology, Tokyo, Japan*

³*Department of Chemical Engineering and Material Science, University of Minnesota, Twin Cities, USA*

⁴*Natural History Museum, University of Oslo, Norway*

⁵*Department of Earth and Environmental Sciences, Columbia University, New York City, USA*

⁶*Lamont-Doherty Earth Observatory, Columbia University, Palisades, USA*

⁷*Department of Applied Physics and Applied Mathematics, Columbia University, New York City, USA*

* *corresponding authors*

1 **The two most abundant minerals in the Earth are lower mantle bridgmanite and ferroper-**
2 **iclase. The bulk modulus of ferropericlase (Fp) softens as iron d-electrons transition from**
3 **a high-spin to low-spin state, affecting the seismic compressional velocity but not the shear**
4 **velocity. Here, we identify a seismological expression of the iron spin crossover in fast regions**
5 **associated with cold Fp-rich subducted oceanic lithosphere: the relative abundance of fast ve-**

6 **locities in P- and S-wave tomography models diverges in the $\sim 1,400\text{-}2,000$ km depth range.**
7 **This is consistent with a reduced temperature sensitivity of P-waves throughout the iron**
8 **spin crossover. A similar signal is also found in seismically slow regions below $\sim 1,800$ km,**
9 **consistent with broadening and deepening of the crossover at higher temperatures. The cor-**
10 **responding inflection in P-wave velocity is not yet observed in 1-D seismic profiles, suggesting**
11 **that non-uniformly distributed thermochemical heterogeneities are present and dampen the**
12 **global signature of the Fp spin crossover.**

13 **1 Introduction**

14 Mineral physics experiments¹⁻³ and theory^{4,5} consistently predict that Fe^{2+} in Fp, $(\text{Mg,Fe})\text{O}$, un-
15 dergoes a high-spin to low-spin (HS-LS) crossover at mid-lower mantle conditions (Fig. 1). Confir-
16 mation of the existence and observation of the iron spin crossover in the Earth's mantle is relevant
17 because it alters material properties such as density, viscosity, elasticity, thermal conductivity, and
18 elemental partitioning in the lower mantle⁶. Slab, plume, and deep mantle dynamics are all thought
19 to be affected by the crossover^{7,8}. In spite of its potential importance, the spin crossover in Fp has
20 thus far eluded seismological detection, suggesting that the predictions are inaccurate, the signa-
21 ture is below the detection threshold, and/or the lower mantle has a lower $(\text{Fe}+\text{Mg})/\text{Si}$ ratio than
22 the shallower mantle.

23 The distinct effects of the Fp spin crossover on compressional (P-waves) and shear (S-waves)
24 wave velocities offer a promising target for geophysical observation (Fig. 2). In particular, a vol-
25 ume reduction during the spin crossover⁴ inevitably increases its compressibility and decreases its

26 bulk modulus⁹. Both the onset pressure as well as pressure interval of the mixed spin region (where
27 both high- and low-spin states coexist) are predicted to increase at higher temperatures^{6,9-11}. The
28 temperature dependence of the pressure onset and pressure range of the HS-LS crossover result in
29 an anomalous dependence of the bulk modulus on temperature¹², with little influence on the shear
30 modulus (Fig. 2a). The magnitude of this effect increases for higher iron contents and abundance
31 of Fp⁶. Specifically, the transition pressure does not significantly change for iron concentrations
32 below $\sim 20\%$ in Fp, which is the case for most Fp-bearing aggregates in the lower mantle¹³.

33 One consequence of the bulk modulus softening during the iron spin crossover in Fp is that
34 the P-wave velocity is generally reduced while the S-wave velocity remains unaffected. Fig. 2
35 shows the effect of the iron spin crossover in Fp on the seismic velocities of a hypothetical pyrolite
36 composition rock. Our *ab initio* mineral physics calculations¹³ use a simplified pyrolite com-
37 position consisting of 78.9 mol% bridgmanite, 14.6 mol% ferropericlase and 6.5 mol% calcium
38 perovskite, with 16 mol% FeO in the Fp. The mantle is thought to be a lithological mix of depleted
39 peridotite and separate slivers and lenses of recycled oceanic crust. Supplementary Fig. 1 shows
40 P-wave and S-wave velocities for Fp-free rock (perovskitite), and Fp-rich harzburgite containing
41 26 mol% Fp, to demonstrate the influence of variable Fp abundances on mid-mantle seismic veloc-
42 ities. The harzburgite composition represents melt-depleted sub-oceanic mantle lithosphere. Most
43 domains in the lower mantle likely contain Fp in the range bounded by these two compositions.
44 The Fe/Mg ratio of Fp in a pyrolitic model composition has been proposed as representative for
45 1-D seismic profiles^{14,15}. However, the compressional velocity of a homogeneous pyrolitic mantle
46 does not fit 1-D seismic models when the effects of the iron spin crossover are included in the

47 predicted seismic velocity computations¹⁶. Our predicted velocity reductions are supported by ex-
48 perimental data⁵, especially from Brillouin scattering^{11,17}. Thus, we survey P-wave and S-wave
49 velocity tomography models for the distinctive seismic signal of the iron spin crossover in Fp:
50 S-velocity anomalies produced by lateral temperature variations persist but P-velocity anomalies
51 weaken within the mixed spin region (see Fig. 2c).

52 In the lower mantle, regions with fast seismic anomalies are commonly interpreted as cold,
53 sinking oceanic lithosphere^{18,19}. These subducted slabs typically comprise 5-7 km of basaltic
54 crust underlain by ~60-80 km of mantle. The lithospheric mantle is depleted in Si due to the
55 extraction of basaltic melt, increasing its Mg/Si ratio and thus the relative amount of Fp in the
56 lithospheric mantle (at lower mantle conditions). Because the magnitude of the velocity reduction
57 due to the iron spin crossover depends on the abundance of Fp (Supplementary Fig. 1), these fast
58 seismic regions should therefore host the strongest spin crossover-related seismic signals. Slow
59 regions in the mid-mantle may be due to return flow of former oceanic plates after becoming warm
60 and buoyant near the core-mantle boundary²⁰. Depending on wavelength and depth, previous
61 comparisons of P- and S-wave tomography models suggest different characteristics in the lower
62 mantle²¹⁻²³, despite similar P- and S-wave coverage and thus similar resolution within the mid-
63 lower mantle^{24,25}. Thus, we focus on characteristics within fast and slow velocity regions in P-wave
64 and S-wave models, both via individual tomography models and combined through tomographic
65 vote maps.

66 2 Results and Discussion

67 **Individual tomography models:** With the rapid expansion of data acquisition and improvements
68 in inversion and modelling techniques in recent decades, numerous global P- and S-wave seismic
69 tomography models are now available^{26–28}. Here we use 4 P-wave models (DETOX-P01²⁹, GAP-
70 P4^{30,31}, HMSL-P06³², MITP-2011³³), and 4 S-wave models (HMSL-S06³², S40RTS³⁴, savani³⁵,
71 SEMUCB-WM1³⁶) that capture a range of global, whole mantle tomographic data and techniques.
72 Fig. 3 shows the overall methodology we use to determine the vertical and lateral extent of fast
73 and slow regions. The percentage of the surface area at each depth that is identified as a fast (or
74 slow) seismic anomaly is calculated as derived from a contour threshold. We define the threshold
75 for fast/slow as seismic wave speed anomalies that exceed one standard deviation (σ) from the
76 mode in the central portion of the seismic velocity distribution over a reference depth range of
77 1,000-2,200 km (i.e., $\geq 1\sigma$ for fast, $\leq -1\sigma$ for slow, see Methods). Supplementary Figs. 2-4 show
78 the resiliency of alternative thresholds for defining fast/slow anomalies of the depth-dependent
79 trends. The surface area of fast and slow wave speed anomalies, plotted at depth intervals of 50
80 km across the lower mantle, reveals distinct patterns between P-wave and S-wave models (Fig. 4),
81 including more variability between the P-wave models than between the S-wave models, as also
82 noted in³⁷. When viewed collectively (Fig. 4), these individual tomography models indicate that
83 the area covered by fast P-wave velocities decreases in the lower mantle across the depth range of
84 $\sim 1,400$ -2,200 km relative to S-wave velocities.

85 **Vote maps:** The differences in the characteristics and distribution of seismic anomalies, both
86 within and between the P-wave and S-wave models, and as illustrated in Fig. 4, lead us to fur-
87 ther inspect the geographic similarity of these patterns. Thus, we employ a vote map method to
88 examine the surface area of fast and slow regions that are common to all of these models³⁸ (Fig.
89 3a-c, see Methods). The highest count (Fig. 1b-c; 4 votes) indicates regions where all four mod-
90 els (P-waves or S-waves) agree on the existence of fast anomalies (i.e. $\geq 1\sigma$) at a given depth
91 interval. For example, the pattern of fast anomaly vote maps (Fig. 5) reveals north-south trending
92 subducted slabs under North America, related to long-lived subduction along eastern Panthalassa,
93 as well east-west trending slabs related to palaeo-subduction within the Tethys Ocean³⁸. Likewise,
94 the cluster analysis-based vote map technique^{37,39} illuminated the common morphology of large
95 low shear velocity provinces (LLSVP) in the lowermost mantle.

96 The vote map procedure does not add any features not already present in the constituent
97 tomography models; it rather highlights the features that are common to multiple models. For
98 example, when analysing global, whole mantle models, it is difficult to know if any given patch
99 of anomalously fast or slow velocity is due to imperfect input data, inversion artefacts, or is a
100 genuine signal present in the lower mantle. Each tomography model utilizes different types of
101 input data, parameterization, regularization, and other subjective choices in their construction (e.g.
102 see model compilations^{28,38,40,41}). Therefore, we expect that features introduced into individual
103 tomography models due to unique tomographic data and/or modeling approaches will not have a
104 strong influence in the highest count of the vote maps (e.g.³⁹). Furthermore, our contour analysis
105 is global and is therefore less susceptible to locally-restricted seismic anomalies. By the same

106 token, vote maps offer a framework for unique, localized anomalies to be identified and evaluated
107 between tomography models.

108 **Vote maps - fast:** Similar to the individual models shown in Fig. 4, the surface area of fast veloc-
109 ity regions in P- and S-wave vote maps (Fig. 1b) diverges in the mid-mantle beginning at $\sim 1,400$
110 km depth. This observed depth is similar to that predicted for the mixed spin region in Fp for a
111 pyrolitic composition, Fig. 1a. The decorrelation of anomalous P-wave and S-wave abundances
112 is a robust signal regardless of the analysis type; contour threshold, highest vote counts, or model
113 combinations. For example, we also test the influence of sequentially adding in the tomography
114 models (from 1 to 4 models) in Supplementary Fig. 5, as well as alternative combinations of 3 of
115 the 4 models in Supplementary Fig. 6. The decorrelation signal of fast P-waves and S-waves was
116 also demonstrated in an earlier vote map paper³⁸ which used an expanded set of 14 tomography
117 models and contoured by the mean of the positive values rather than standard deviation. Further-
118 more, in Supplementary Fig. 7 we compare the depth-dependent signal when using lower vote
119 counts rather than just the maximum vote count of 4 in Fig. 1b,c. These tests demonstrate the
120 robustness of the P- versus S-wave signal.

121 **Vote maps - slow:** To further test the hypothesis that the decoupling of the fast velocity signals
122 in P-wave and S-wave models reflects a spin crossover in Fp, we examine seismically slow, and
123 presumably warm, portions of tomographic models. The surface area of slow velocity regions in
124 the vote maps (Fig. 1c) reveals that the onset of divergence shifts to greater depths (i.e. below
125 $\sim 1,800$ km) consistent with the deepening of the spin crossover as temperature increases (Fig. 1a).

126 It also demonstrates the predicted broadening of the spin transition at higher temperatures (Fig.
127 1a), leading to a more diffuse seismic signal. The divergence in slow velocity regions between
128 P- and S-wave models is likewise more subtle than that observed in fast velocity regions, see also
129 Supplementary Fig. 5-6. The vote maps are a useful tool for examining these types of subtle but
130 consistent and geographically coherent velocity anomaly patterns, i.e., the common signal derived
131 from slow anomalies in the individual tomography models (Fig. 4) is more discernible in the vote
132 maps (Fig. 1b,c).

133 Figs. 5-6 show horizontal and vertical cross-sections, respectively, through vote maps of fast
134 and slow velocity regions. All vote values are shown in these images (i.e. 0-4 votes). We can
135 qualitatively observe a divergence in the agreement among P-wave models compared to S-wave
136 models in the mid mantle for both fast and slow anomalies. For example, fast anomalies attributed
137 to subducted slabs under North America and SE-Asia appear contiguous through the mid-mantle
138 in S-wave vote maps. However, the P-wave vote maps show a weakening of the fast seismic signal
139 in the mid mantle (coherent subducted lithosphere at the top and bottom of the lower mantle is
140 still observed). Likewise, the slow mantle domain under Africa and the Afar hotpot region is
141 more readily apparent in S-wave than in P-wave vote maps towards the lowermost mantle. This
142 observed interference is what is predicted for the spin crossover in Fp^{12} . The disruption of slab
143 and plume images in the mid-mantle has also been noted in other studies ^{22,42-46}. Fig. 7 shows
144 difference maps, highlighting the spatial and depth-dependent differences between the P- and S-
145 wave vote maps. There is a dominance of S-wave votes over P-wave votes in the lowermost mantle,
146 especially for the fast anomalies in regions of long-lived subduction (Figs. 5 and 6), and in the slow

147 anomalies for regions corresponding to the LLSVP domains.

148 We note that the abundance of fast velocity regions in both P-wave and S-wave models (Fig.
149 1b, 4) increases below $\sim 2,500$ km depth, with the area of fast S-wave anomalies increasing rapidly
150 toward the base of the mantle. This relative difference between fast S- and P-wave anomalies near
151 the core-mantle boundary is likely caused by the appearance of post-perovskite in cold mantle,
152 which is expected to increase S-wave velocity by $\sim 1-2\%$ but has notably smaller effect on P-
153 waves⁴⁷⁻⁴⁹. The difference maps between P-wave and S-wave velocities at 2,800 km depth, shown in
154 Fig. 7, reveal regions of potential post-perovskite (dark purple regions indicating higher S-wave
155 velocities than P-wave velocities). The antipodal LLSVPs, beneath the Pacific and Africa, are areas where
156 the S-wave velocity is greatly reduced relative to the P-velocity at the base of the mantle ($\sim 2,700$
157 km). The divergence between S- and P-wave behaviours within the LLSVPs has been used to
158 argue for the presence of dense chemically distinct piles in these regions⁵⁰.

159 **Effect of iron partitioning:** The spin crossover is expected to influence the iron partitioning (K_D)
160 between bridgmanite (Bm), $(\text{Mg,Fe,Al,Si})\text{O}_3$, and $\text{Fp}^{1,51}$ by increasing the mole% of FeO in Fp,
161 thus decreasing K_D ⁵¹. Since the spin crossover may shift to higher pressures as K_D decreases⁶, the
162 pressure range over which the crossover occurs could be wider than that predicted for the constant
163 partitioning value of $K_D=0.5$ which we assign in our calculations. We also investigated how the
164 onset and depth range of the spin crossover changes with variable K_D ⁵¹ values (Supplementary Fig.
165 8). The velocities with variable K_D are barely distinguishable from the constant K_D case due to a
166 very weak dependence on the crossover depth on FeO content below ~ 20 mole% (e.g.^{52,53}). This

167 prediction is consistent with our observation that the effects of the crossover on P-velocities in fast
168 velocity regions does not extend below ~ 2500 km depth for Fp-rich compositions, Supplementary
169 Fig. 1.

170 **Implications for lower mantle composition:** A reduction in the mid-mantle fast velocity regions
171 in P-wave models compared to S-wave models is consistent with the predictions of an iron spin
172 crossover in Fp. Due to uncertainties in the average mantle geotherm¹⁶ we compare our predicted
173 P- and S-wave velocities to the Preliminary Reference Earth Model (PREM)⁵⁴ radial P-wave profile
174 using a temperature profile that aligns the predicted S-wave velocity to PREM, Fig. 1d. These
175 predictions for a pyrolite composition demonstrate that the spin crossover signal could be present
176 in 1-D seismic profiles if the lower mantle had an adiabatic temperature profile and Fp-bearing
177 composition. However, the intensity of the P-wave velocity reduction depends on the Fp abundance
178 and the abundance of iron in the Fp which could be different than our model composition. Since
179 Bm has a similar spin crossover for ferric iron (Fe^{3+}) located in the octahedral B-site⁵⁵, the lack
180 of a distinct iron crossover in the lower mantle⁵⁶ suggests that aluminium displaces Fe^{3+} from the
181 B-site⁵⁷. While there are still uncertainties on the spin crossover pressure range and magnitude of
182 the seismic signal at the highest mantle temperatures, the general agreement between theoretical
183 predictions⁵ and experimental measurements¹¹ at room temperature compels us to consider how
184 to reconcile the patterns observed here, in both the fast and slow regions, with those from the 1-D
185 average profiles.

186 The observed divergence in P-wave and S-wave models in the fastest and slowest regions

187 of the mid-mantle indicates that the iron spin crossover signal is seismically detectable in mantle
188 regions expected to have peridotitic-to-pyrolitic compositions. Variable composition, such as re-
189 gions with less Fp than pyrolite or less iron in the Fp, could disrupt and reduce the spin crossover
190 signal^{10,16}. Lateral temperature variations introduce a depth dependence to the P-wave seismic
191 velocity inflection, which could reduce the globally averaged signal. Geodynamically, the lack
192 of a ubiquitous signal of the iron spin crossover in the lower mantle may indicate that sluggish
193 mantle mixing has yet to erase large-scale heterogeneities. The concentration of Fp in the fastest
194 and slowest regions of the lower mantle is complementary to high viscosity thus likely Fp-poor
195 regions occupying large domains of the lower mantle^{20,58}. In addition, 1-D seismic models using
196 low-order polynomial parameterizations of radial velocities may have smoothed the seismic signal
197 of the iron spin crossover which becomes more subdued as the shape and distribution of thermo-
198 chemical provinces becomes more varied. High resolution regional 1-D profiles are challenging
199 to construct but would reveal the presence or absence of Fp outside of regions with large lateral
200 temperature variations such as those identified in this study. Further analysis is needed to more
201 fully address the range of scales and compositions that could jointly satisfy mineral physics and
202 seismic constraints.

203 Our study qualitatively identifies the predicted seismic expression of the iron spin crossover
204 in lower mantle Fp in fast and slow regions of global tomography models. The effects of the
205 iron spin crossover on seismic velocities are subtle but most discernible in the presence of lateral
206 temperature variations in Fp-bearing regions that extend across the depths that span the iron spin
207 crossover range. Uniquely identifying Fp in the fastest and slowest regions without a strong signal

208 in the global average mantle suggests the presence of a mosaic of large-scale temperature and
209 composition variations in the lower mantle.

210 3 Methods

211 **Predictions of the Spin Crossover in Fp.** Fig. 1a was calculated for $\text{Mg}_{1-x}\text{Fe}_x\text{O}$ with $x=18.75\%$
212 using published models^{5,12}. The low spin fraction is calculated as:

$$n(P, T) = \frac{1}{1 + m(2S + 1) \exp \left[\frac{\Delta G_{\text{HS-Ls}}^{\text{st+vib}}}{X_{\text{Fe}} k_B T} \right]} \quad (1)$$

213 where $m = 3$ for the three possible orientations of minority electron d orbital (xy, yz, or zx) and S
214 = 2. $\Delta G_{\text{HS-Ls}}^{\text{st+vib}}$ includes only static and vibrational energy, without electronic entropy. Our elas-
215 tic moduli and densities are also taken from published models^{5,13,59,60}. These calculations used
216 the rotationally invariant local density approximation LDA+U_{SC} method calculated with a self-
217 consistent Hubbard U⁶¹. Results for Fp were obtained using a 64-atom supercell with an iron
218 concentration of $x=18.75\%$ (24 Mg, 32 O, and 6 Fe maximally separated from each other). Ther-
219 moelastic properties were then obtained for other concentrations by linearly interpolating between
220 $x=0$ and $x=18.75\%$. The vibrational density of states (VDOS) was computed using the vibrational
221 virtual-crystal model⁹, and then used in conjunction with the quasiharmonic approximation to pre-
222 dict high temperature effects. The magnitude of the predicted effects are in good agreement with
223 experimental measurements¹¹. Thermoelastic properties from^{59,60} are used for Fe^{2+-} , Fe^{3+-} and
224 Al-bearing bridgmanite.

225 The mantle is thought to be a lithological mix of depleted peridotite and separate slivers and

	SiO ₂	MgO	FeO	CaO	Al ₂ O ₃
Harzburgite	43.52 (36.07)	45.73 (56.51)	8.76 (6.07)	0.91 (0.81)	1.09 (0.53)
Peridotite	44.48 (38.50)	39.22 (50.61)	8.1 (5.86)	3.44 (3.19)	3.59 (1.83)
Pyrolite	45.00 (39.37)	37.80 (49.30)	8.05 (5.89)	3.55 (3.33)	4.09 (2.11)
Fp-free model	54.79 (48.91)	30.11 (40.06)	7.85 (5.86)	3.11 (2.97)	4.14 (2.18)

Table 1: Compositions used in this study and in ¹³ in wt.% (mole %). The velocities, elastic moduli, and self consistent thermal profiles (isentropes) for harzburgite⁶², pyrolite^{63,64}, peridotite⁶⁵, and an Fe-free model composition⁶⁴ are derived from recent *ab initio* calculations¹³ which incorporate the effects of the iron spin crossover in Fp. The signature of the spin crossover in peridotite occurs at a similar pressure and temperature range as for pyrolite for the same geotherm.

226 lenses of recycled oceanic crust (ROC). Whereas the current subduction zones have an average
227 ROC to depleted peridotite ratio of about 1/10, this ratio has probably decreased steadily from
228 larger ROC fractions in the Archean (e.g. ⁶⁶). Although a depleted peridotite has higher Fp-content
229 with higher Fe/Mg ratio than a fertile (pyrolitic) peridotite ⁵¹, presumably resulting in a slightly
230 stronger spin crossover signal, this effect will be weakened by the diluting ROC content.

231 The shear and bulk modulus (Fig. 2a), S-wave (Fig. 2b) and P-wave velocity (Fig. 1d, 2c) are
232 calculated for a pyrolite⁶³ composition. The self consistent geotherms are calculated by setting the
233 starting temperature of the calculation at the top of the lower mantle to 1373 K (the -500 K case),
234 1873 (the average case), and 2373 K (the +500 K case) (Supplementary Fig. 8 and 9). The oxide
235 components (Table 1) are 45 wt.% SiO₂, 38 wt.% MgO, 8 wt.% FeO, 4 wt.% CaO, and 4 wt.%
236 Al₂O₃, and the rock mineralogy is 76 mole% bridgmanite, 17 mole% ferropericlase, and 7 wt.%
237 calcium perovskite. The calculations for peridotite (Table 1) are the same, but with 6 mole% CaO.
238 Ferropericlase, (Mg_{0.85}Fe_{0.15})O, hosts 15 mol% FeO¹³. The Earth's actual mantle geotherm is
239 uncertain, and fitting PREM requires non-adiabatic gradients and/or variations in composition with
240 depth in the lower mantle⁶⁷. Here the P-wave velocity in Fig. 1d is calculated using temperatures
241 that align pyrolite S-wave velocity to PREM⁵⁴ at each depth, thus highlighting the inability to
242 match both S-wave and P-wave constraints simultaneously when the effects of a spin crossover are
243 included (S-wave velocities are not significantly affected by the spin crossover, Fig. 2b). Note, that
244 this calculation is performed for an averaged chemical composition without lateral temperature
245 variations.

246 **Fast and slow mapping** Most tomography models agree on the large-wavelength structure of
247 seismic velocity anomalies in the mantle e.g.^{34,39,42}. However, the amplitudes of the anomalies,
248 as well as smaller scale-features such as individual subducted slabs, sometimes vary owing to
249 differences in parameterization, data processing, regularization, and other subjective influences²².
250 There are also few joint P- and S-wave models that do not include some type of scaling of the
251 P-wave model to the S-wave model in the lower mantle. Finally, wide disparities in amplitudes
252 have been noted between various models⁴¹, which may reflect volume and coverage of data, choice
253 of regularization parameters, volume discretization, and other influences (Supplementary Fig. 10).

254 Instead of relying on particular P- and S-wave model pairs and their stated amplitudes, we set
255 a uniform grid in the mantle and generate a contour based on a given positive/negative σ deviation
256 for fast/slow anomalies, respectively. We define σ for each model by combining and binning all
257 values between 1,000 km and 2,200 km depth (by area) to produce a mid-mantle reference distri-
258 bution. We use only the mid-mantle to avoid more complex behaviours that appear in the shallow
259 and deep portions of the lower mantle. We then perform an iterative Gaussian fitting procedure⁴¹
260 on the mid-mantle reference distribution, utilizing values only within the interval $-1 < \sigma < 1$. This
261 procedure avoids the influence of more extreme velocity values on determining the threshold, as
262 these may exhibit non-normal characteristics that would otherwise exert a large influence on the
263 usual arithmetic measure of standard deviation (Supplementary Figs. 10, 11). If the distribution
264 is perfectly normal, then the σ value obtained using this procedure would be identical to the usual
265 measure of standard deviation. Note that this procedure also excludes what will come to be defined
266 as "fast" or "slow" anomalies from the determination of what constitutes fast or slow velocities;

267 only the dominant modal variation of relatively modest velocity variations is used to obtain σ for
268 each model. Supplementary Fig. 10 shows the mid-mantle reference distributions for all of the
269 models used in this study, along with the Gaussian fits we obtain in the $-1 < \sigma < 1$ intervals. Sup-
270 plementary Fig. 11 shows that the gaussian fitting procedure does not affect the relative variation
271 of seismic velocities in the models, it only serves to bring them into alignment and enables their
272 core velocity variations to exhibit similar amplitudes.

273 **Vote maps** Vote maps are a simple tool, developed to detect the existence and map the distribution
274 of material exhibiting particular seismic characteristics in the lower mantle. Lekic et al.³⁹ and
275 Cottaar and Lekic³⁷ developed a k-means cluster analysis-style vote map for the lower mantle.
276 This was expanded in Shephard et al.³⁸, who developed an alternative vote map technique using
277 tomography and depth-dependent metrics which aimed at surveying individual model depths across
278 the whole mantle and retaining geometric features (see also Hosseini et al.²⁸).

279 The tomography models used in this study were chosen to capture a variety of data types
280 and processing techniques that are employed in tomographic inversions. The 4 P-wave models are
281 DETOX-P01²⁹, GAP-P4^{30,31}, HMSL-P06³², MITP-2011³³, and the 4 S-wave models are HMSL-
282 S06³², S40RTS³⁴, savani³⁵, SEMUCB-WM1³⁶. We refer to the original vote maps paper³⁸ which
283 applied a similar process but to an expanded set of 7 P-wave and 7 S-wave models, and contoured
284 by the mean of the positive values. The original models are not filtered to exclude any spherical har-
285 monic degrees, and can be accessed via the SubMachine website²⁸ <http://submachine.earth.ox.ac.uk/>.

286 As outlined in the original vote map methodology adapted here³⁸, the individual tomography

287 models are linearly interpolated along a 0.5° grid with a depth increment of 50 km. Processing
288 was done with Generic Mapping Tools (GMT, version 5.3.1⁶⁸). The vote map methodology uses
289 sigma values (standard deviation) as the contour metric for each tomography model at each depth
290 (i.e.⁴¹). Each model contributes one vote at each grid cell according to whether the model value
291 lies inside (vote=1) or outside (vote=0) the specified contour. Supplementary Fig. 4 shows an
292 example of the vote map contouring procedure for each tomography model (also applicable to the
293 non-vote maps). Votes for each of the 4 models are tabulated to generate the final vote map grid
294 as shown in Fig. 5. The resulting abundance profiles (in % of area) of agreement (i.e. how many
295 models agree at a given depth, where 4 votes is the maximum agreement) for alternative sigma
296 thresholds for the individual seismic tomography models are shown Supplementary Figs. 2-3. Two
297 additional tomography models TX2019⁶⁹ and SP12RTS⁷⁰ which show higher variability than the
298 models chosen in our analysis, are included for comparison (Supplementary Fig. 12). They were
299 constructed with different data and with different purposes, to image the core-mantle boundary for
300 SP12RTS and to test the influence on subducting slabs for TX2019, which may not make them
301 ideal for our focus on the mid-mantle. Scientific, perceptually uniform colour maps^{71,72} were used
302 in all figures.

303 **Data Availability** The datasets generated and/or analysed during the current study are available at
304 Zenodo [will be updated upon acceptance], temporary file link:

305 http://folk.uio.no/gracees/Shephard_etal_2020_Submitted/

306 **Author contributions** G.E.S., C.H., J.W.H., R.G.T. and R.M.W. instigated the study. G.E.S. and
307 J.W.H. undertook the map preparation, C.H. and R.M.W. undertook the seismic velocity cal-
308 culations, R.M.W. and J.J.V-C. computed elastic moduli and seismic velocities. All authors con-
309 tributed to the scientific discussion and preparation of the manuscript.

4 References

1. Badro, J. *et al.* Iron partitioning in Earth's mantle: Toward a deep lower mantle discontinuity. *Science* **300**, 789–791 (2003).
2. Fei, Y. *et al.* Spin transition and equations of state of (Mg,Fe)O solid solutions. *Geophys. Res. Lett.* **34**, L17307 (2007).
3. Komabayashi, T., Hirose, K., Nagaya, Y., Sugimura, E. & Ohishi, Y. High-temperature compression of ferropicicase and the effect of temperature on iron spin transition. *Earth Planet. Sci. Lett.* **297**, 691–699 (2010).
4. Tsuchiya, T., Wentzovitch, R. M., da Silva, C. R. S. & de Gironcoli, S. Spin transition in magnesiowüstite in Earth's lower mantle. *Phys. Rev. Lett.* **96**, 198501 (2006).
5. Wu, Z., Justo, J. & Wentzovitch, R. Elastic anomalies in a spin-crossover system: Ferropicicase at lower mantle conditions. *Phys. Rev. Lett.* **110**, 228501 (2013).
6. Lin, J.-F., Speziale, S., Mao, Z. & Marquardt, H. Effects of the electronic spin transitions of iron in lower mantle minerals: Implications for deep mantle geophysics and geochemistry. *Reviews of Geophysics* **51**, 244–275 (2013).

7. Shahnas, M., Pysklywec, R., Justo, J. & Yuen, D. A. Spin transition-induced anomalies in the lower mantle: implications for mid-mantle partial layering. *Geophysical Journal International* **210**, 765–773 (2017).
8. Bower, D. J., Gurnis, M., Jackson, J. M. & Sturhahn, W. Enhanced convection and fast plumes in the lower mantle induced by the spin transition in ferropericlae. *Geophysical Research Letters* **36**, 10 (2009).
9. Wentzcovitch, R. *et al.* Anomalous compressibility of ferropericlae throughout the iron spin crossover. *Proc. Natl. Acad. Sci. USA* **106**, 8447–8452 (2009).
10. Wu, Z. & Wentzcovitch, R. Composition versus temperature induced velocity heterogeneities in a pyrolitic lower mantle. *Earth Planet. Sci. Lett.* **457**, 359–365 (2017).
11. Marquardt, H. *et al.* Elastic softening of (Mg_{0.8}Fe_{0.2})O ferropericlae across the iron spin crossover measured at seismic frequencies. *Geophys. Res. Lett.* **45**, 6862–6868 (2018).
12. Wu, Z. & Wentzcovitch, R. Spin crossover in ferropericlae and velocity heterogeneities in the lower mantle. *Proc. Nat. Acad. Sci.* **111**, 10468–10472 (2014).
13. Valencia-Cardona, J. *et al.* Influence of the iron spin crossover in ferropericlae on the lower mantle geotherm. *Geophys. Res. Lett.* **44**, 4863–4871 (2017).
14. Mattern, E., Matas, J., Ricard, Y. & Bass, J. Lower mantle composition and temperature from mineral physics and thermodynamic modelling. *Geophys. J. Int.* **160**, 973–990 (2005).

15. Wang, X., Tsuchiya, T. & Hase, A. Computational support for a pyrolytic lower mantle containing ferric iron. *Nature Geoscience* **8**, 556–560 (2015).
16. Houser, C., Hernlund, J., Valencia-Cardona, J. & Wentzcovitch, R. Discriminating lower mantle composition. *Phys. Earth Planet. Int.* **308**, 106552 (2020).
17. Marquardt, H., Speziale, S., Reichmann, H. J., Frost, D. J. & Schilling, F. R. Single-crystal elasticity of (mg_{0.9}fe_{0.1})o to 81gpa. *Earth and Planetary Science Letters* **287**, 345 – 352 (2009).
18. Grand, S. Mantle shear-wave tomography and the fate of subducted slabs. *Phil. Trans. R. Soc. Lond. A* **360**, 2475–2491 (2002).
19. Ishii, M. & Tromp, J. Normal-mode and free-air gravity constraints on lateral variations in velocity and density of earth’s mantle. *Science* **285**, 1231–1236 (1999).
20. Ballmer, M., Houser, C., Hernlund, J., Wentzcovitch, R. & Hirose, K. Persistence of strong silica-enriched domains in the Earth’s lower mantle. *Nature Geoscience* **10**, 236–240 (2017).
21. Saltzer, R. L., van der Hilst, R. D. & Karason, H. Comparing P and S wave heterogeneity in the mantle. *Geophys. Res. Lett.* **28**, 1335–1338 (2001).
22. Houser, C. & Williams, Q. The relative wavelengths of fast and slow velocity anomalies in the lower mantle: Contrary to the expectations of dynamics? *Phys. Earth Planet. Int.* **176**, 187–197 (2009).

23. Antolik, M., Gu, Y. J., Ekström, G. & Dziewonski, A. M. J362D28: a new joint model of compressional and shear velocity in the Earth's mantle. *Geophysical Journal International* **153**, 443–466 (2003).
24. Mora, S. D., Boschi, L., Tackley, P. J., Nakagawa, T. & Giardini, D. Low seismic resolution cannot explain S/P decorrelation in the lower mantle. *Geophys. Res. Lett.* **38**, L12303 (2011).
25. Moulik, P. & Ekström, G. The relationships between large-scale variations in shear velocity, density, and compressional velocity in the Earth's mantle. *J. Geophys. Res.* **121**, 2327–2771 (2016).
26. van der Hilst, R., Widiyantoro, S. & Engdahl, E. Evidence for deep mantle circulation from global tomography. *Nature* **386**, 578–584 (1997).
27. Simmons, N. A., Myers, S. C., Johannesson, G. & Matzel, E. LLNL-G3Dv3: Global P wave tomography model for improved regional and teleseismic travel time prediction. *J. Geophys. Res.* **117** (2012).
28. Hosseini, K. *et al.* Submachine: Web-based tools for exploring seismic tomography and other models of Earth's deep interior. *Geochem. Geophys. Geosys.* **19**, 1464–1483 (2018).
29. Hosseini, K. & Sigloch, K. Multifrequency measurements of core-diffracted P waves (Pdiff) for global waveform tomography. *Geophys. J. Int.* **203**, 506–521 (2015).
30. Obayashi, M. *et al.* Finite frequency whole mantle P wave tomography: Improvement of subducted slab images. *Geophys. Res. Lett.* **40**, 5652–5657 (2013).

31. Fukao, Y. & Obayashi, M. Subducted slabs stagnant above, penetrating through, and trapped below the 660 km discontinuity. *J. Geophys. Res.* **118**, 5920–5938 (2013).
32. Houser, C., Masters, G., Shearer, P. & Laske, G. Shear and compressional velocity models of the mantle from cluster analysis of long-period waveforms. *Geophys. J. Int.* **174**, 195–212 (2008).
33. Burdick, S. *et al.* Model update March 2011: Upper mantle heterogeneity beneath North America from traveltimes tomography with global and USArray Transportable Array data. *Seismological Research Letters* **83**, 23–28 (2012).
34. Ritsema, J., Deuss, A., van Heijst, H. J. & Woodhouse, J. H. S40RTS: A degree-40 shear-velocity model for the mantle from new Rayleigh wave dispersion, teleseismic traveltimes and normal-mode splitting function measurements. *Geophys. J. Int.* **184**, 1223–1236 (2011).
35. Auer, L., Boschi, L., Becker, T. W., Nissen-Meyer, T. & Giardini, D. Savani: A variable resolution whole-mantle model of anisotropic shear velocity variations based on multiple data sets. *J. Geophys. Res.* **119**, 3006–3034 (2014).
36. French, S. W. & Romanowicz, B. A. Whole-mantle radially anisotropic shear velocity structure from spectral-element waveform tomography. *Geophys. J. Int.* **199**, 1303–1327 (2014).
37. Cottaar, S. & Lekic, V. Morphology of seismically slow lower-mantle structures. *Geophysical Journal International* **207**, 11221136 (2016).
38. Shephard, G., Matthews, K., Hosseini, K. & Domeier, M. On the consistency of seismically imaged lower mantle slabs. *Science Reports* **7**: 10976 (2017).

39. Lekic, V., Cottaar, S., Dziewonski, A. & Romanowicz, B. Cluster analysis of global lower mantle tomography: A new class of structure and implications for chemical heterogeneity. *Earth Planet. Sci. Lett.* **357358**, 6877 (2012).
40. Becker, T. W. & Boschi, L. A comparison of tomographic and geodynamic mantle models. *Geochemistry, Geophysics, Geosystems* **3** (2002).
41. Hernlund, J. & Houser, C. On the distribution of seismic velocities in Earth's deep mantle. *Earth Planet. Sci. Lett.* **265**, 423–437 (2008).
42. Masters, G., Laske, G., Bolton, H. & Dziewonski, A. The relative behavior of shear velocity, bulk sound speed, and compressional velocity in the mantle: Implications for chemical and thermal structure. In i. Karato, S., Forte, A., Liebermann, R., Masters, G. & Stixrude, L. (eds.) *Earth's Deep Interior: Mineral Physics and Tomography From the Atomic to Global Scale*, 63–87 (American Geophysical Union Monograph, 2000).
43. Montelli, R., Nolet, G., Dahlen, F., Masters, G. & Engdahl, E. Finite-frequency tomography reveals a variety of plumes in the mantle. *Science* **303**, 338–343 (2004).
44. Boschi, L., Becker, T. W. & Steinberger, B. On the statistical significance of correlations between synthetic mantle plumes and tomographic models. *Physics of the Earth and Planetary Interiors* **167**, 230 – 238 (2008).
45. Simmons, N. A., Forte, A. M., Boschi, L. & Grand, S. P. Gypsum: A joint tomographic model of mantle density and seismic wave speeds. *Journal of Geophysical Research: Solid Earth* **115** (2010).

46. Koelemeijer, P., Schuberth, B., Davies, D., Deuss, A. & Ritsema, J. Constraints on the presence of post-perovskite in earth's lowermost mantle from tomographic-geodynamic model comparisons. *Earth and Planetary Science Letters* **494**, 226–238 (2018).
47. Tsuchiya, T., Tsuchiya, J., Umemoto, K. & Wentzcovitch, R. Elasticity of mgsio₃ post-perovskite. *Geophys. Res. Lett.* **31**, L14603 (2004).
48. Wentzcovitch, R. M., Tsuchiya, T. & Tsuchiya, J. MgSiO₃ postperovskite at D'' conditions. *Proc. Nat. Acad. Sci.* **103**(3), 543–546 (2006).
49. Hutko, A., Lay, T., Revenaugh, J. & Garnero, E. Anticorrelated seismic velocity anomalies from post-perovskite in the lowermost mantle. *Science* **320**, 1070–1074 (2008).
50. Garnero, E., McNamara, A. & Shim, S.-J. Continent-sized anomalous zones with low seismic velocity at the base of Earth's mantle. *Nature Geoscience* **9**, 481–489 (2016).
51. Piet, H. *et al.* Spin and valence dependence of iron partitioning in Earth's deep mantle. *Proc. Nat. Acad. Sci.* **113** (40), 11,127–11,130 (2016).
52. Tsuchiya, T., Wentzcovitch, R., da Silva, C., de Gironcoli, S. & Tsuchiya, J. Pressure induced high spin to low spin transition in magnesiowstite. *Phys. Stat. Sol. (b)* **243**, 2111–2116 (2006).
53. Persson, K., Bengtson, A., Ceder, G. & Morgan, D. Ab initio study of the composition dependence of the pressure-induced spin transition in the (Mg_{1-x},Fe_x)O system. *Geophys. Res. Lett.* **33**, L16306 (2006).

54. Dziewonski, A. & Anderson, D. Preliminary reference Earth model. *Phys. Earth Planet. Inter.* **25**, 297–356 (1981).
55. Hsu, H., Blaha, P., Cococcioni, M. & Wentzcovitch, R. Spin-state crossover and hyperfine interactions of ferric iron in MgSiO₃ perovskite. *Physical Review Letters* **106** (2011).
56. Liu, J. *et al.* Valence and spin states of iron are invisible in earths lower mantle. *Nature communications* **9:1**, 1–9 (2017).
57. Hsu, H., Yu, Y. & Wentzcovitch, R. Spin crossover of iron in aluminous MgSiO₃ perovskite and post-perovskite. *Earth and Planetary Science Letters* **359**, 34–39 (2012).
58. Rudolph, M., Lekic, V. & Lithgow-Bertelloni, C. Viscosity jump in earth's mid-mantle. *Science* (2015).
59. Shukla, G. *et al.* Thermoelasticity of Fe²⁺-bearing bridgmanite. *Geophys. Res. Lett.* **42**, 1741–1749 (2015).
60. Shukla, G., Cococcioni, M. & Wentzcovitch, R. Thermoelasticity of Fe³⁺- and Al-bearing bridgmanite: Effects of iron spin crossover. *Geophys. Res. Lett.* **43**, 5661–5670 (2016).
61. Kulik, H. J., Cococcioni, M., Scherlis, D. A., & Marzari, N. Density functional theory in transition-metal chemistry: A self-consistent Hubbard U approach. *Physical Review Letters* **97** (2006).
62. Baker, M. B. & Beckett, J. R. The origin of abyssal peridotites: A reinterpretation of constraints based on primary bulk compositions. *Earth Planet. Sci. Lett.* **171**, 49–61 (1999).

63. McDonough, W. F. & Sun, S. The composition of the Earth. *Chemical Geology* **120**, 223–253 (1995).
64. Williams, Q. & Knittle, E. The uncertain major element bulk composition of Earth's mantle. *Earth's Deep Mantle: Structure, Composition, and Evolution. Geophysical Monograph Series 160. AGU* (2005).
65. Hirose, K. & Kushiro, I. Partial melting of dry peridotites at high pressures: Determination of compositions of melts segregated from peridotite using aggregates of diamond. *Earth Planet. Sci. Lett.* **114**, 477489 (1993).
66. Herzberg, C., Condie, K. & Korenaga, J. Thermal history of the earth and its petrological expression. *Earth and Planetary Science Letters* **292**, 79 – 88 (2010).
67. Cobden, L. *et al.* Thermochemical interpretation of 1-D seismic data for the lower mantle: The significance of nonadiabatic thermal gradients and compositional heterogeneity. *J. Geophys. Res.* **114**, doi:10.1029/2008JB006262 (2009).
68. Wessel, P., Smith, W., Scharroo, R., Luis, J. & Wobbe, F. Generic Mapping Tools: Improved Version Released. *EOS Transactions* **94**, 409–420 (2013).
69. Lu, C., Grand, S. P., Lai, H. & Garnero, E. J. TX2019slab: A new P and S tomography model incorporating subducting slabs. *Journal of Geophysical Research: Solid Earth* **124**, 11549–11567 (2019).

70. Koelemeijer, P., Ritsema, J., Deuss, A. & van Heijst, H.-J. SP12RTS: A degree-12 model of shear- and compressional-wave velocity for Earth's mantle. *Geophysical Journal International* **204**, 1024–1039 (2016).
71. Cramer, F. Geodynamic diagnostics, scientific visualisation and StagLab 3.0. *Geosci. Model Dev.* **11**, 2541–2562 (2018).
72. Cramer, F., Shephard, G. & Heron, P. J. The misuse of colour in science communication. *Nature Communications* **11** (2020).
73. Mueller, R. D. *et al.* Ocean basin evolution and global-scale plate reorganization events since pangea breakup. *Annual Review of Earth and Planetary Sciences* **44**, 107–138 (2016).

Acknowledgements G.E.S. and R.G.T. acknowledge support from the Research Council of Norway through its Centers of Excellence funding scheme, Project Number 223272. C.H. and J.W.H. were primarily supported by the WPI-funded Earth-Life Science Institute at Tokyo Institute of Technology as well as additional support through JSPS KAKENHI grant numbers 15H05832, 16H06285, and 19K04035. R.M.W. and J.J.V-C. were funded through NSF grants EAR-1319361 and EAR1918126. G.E.S. dedicates this work to the memory of Mark A. Shephard.

Competing Interests The authors declare that they have no competing financial interests.

Correspondence Correspondence regarding the mineral physics should be addressed to R.M.W: rmw2150@columbia.edu. All other requests and correspondence should be addressed to G.E.S: grace.shephard@geo.uio.no.

Figure 1 Comparison of mineral physics predictions and seismological observations of the Fe spin crossover in Fp. (a) The depth-temperature distribution of low-spin Fe and three schematic mantle geotherms. The onset of the mixed spin region occurs at shallower depths for relatively colder temperatures and at greater depths and over a broader range at higher temperatures. Surface area of fast (b) and slow (c) velocities in the lower mantle imaged by unanimous consensus (4/4 models) corresponding to the vote maps shown in Figs. 5 and 6. A divergence in the seismic signal between P-wave models relative to S-wave models is revealed below the respective “onset” depths of approximately 1,400 km and 1,800 km. (d) The calculated¹³ profile of P-wave velocities for pyrolite using temperatures that fit S-wave velocities to PREM⁵⁴ reveals a significant departure suggesting that the signature of the spin crossover is not a globally-averaged feature. See Methods. Colour maps from⁷¹.

Figure 2 Depth dependence of elastic moduli and seismic velocities for pyrolite⁶³ containing 17 wt.% Fp with 16 mol% of FeO, 76 wt.% bridgmanite, and 7 wt.% calcium perovskite¹³. (a) Shear and bulk moduli. The anomalous behaviour of the bulk modulus, K ,⁹ ($K = -V(dP/dV)$, where V is volume and P is pressure) is due to the iron octahedron volume collapse during the spin-state change⁴ associated with the spin crossover. As previously shown⁹, the pressure onset, the pressure range of the HS-LS crossover, and associated anomalies in K are temperature dependent (same legend all panels). The shear modulus, G , ($G = \tau/\gamma$, where τ is the shear stress and γ is the shear strain) is not significantly affected by the octahedron volume reduction and increases monotonically

with increasing pressure and decreasing temperature. (b) S-wave ($V_s = \sqrt{G/\rho}$) and (c) P-wave ($V_p = \sqrt{(K + 4/3G)/\rho}$) velocity for pyrolite at different temperatures. The average mantle temperature profile (black) is calculated by setting the starting temperature to 1873 K at 660 km, and integrating the adiabatic temperature gradient¹³ through the lower mantle. The blue/magenta curves were calculated using the same technique, but decreasing/increasing the temperature at 1873 km by ± 500 K. In the mixed-spin region, the softening of K^9 causes a reduction in P-wave velocity sensitivity to isobaric temperature variations¹², while the S-wave velocity remains sensitive to such temperature variations. Consequently, the expected seismic signal of Fp in the lower mantle consists of a disruption of vertically coherent thermal structures in P-velocities, whereas a coherent thermal structure is apparent in the S-velocities^{10,12}. Alternative compositions shown in Supplementary Fig. 1

Figure 3 Workflow used in this paper. Step 1: select tomography model. Step 2: a gaussian fitting procedure is applied (see Methods). Step 3: a contour metric is chosen e.g. fast ($>+1\sigma$ from the mean), and slow ($<-1\sigma$ from the mean) and binary grids are created. Step 4: surface area coverage of the contour is extracted across the lower mantle. For the vote map methodology additional steps are applied between Steps 3-4. Step 3a: binary grids from additional tomography models are created as per Steps 1-3. Step 3b: at each grid point the constituent models (here 4 models) are summed. Step 3c: difference vote maps can be generated, for example by subtracting the S-wave votes from the P-wave votes.

Figure 4 The depth-dependent changes in surface area for the (a) fast ($>+1\sigma$ from the mean), and (b) slow ($<-1\sigma$ from the mean) regions, as applied individually to each of the the 4 P-wave, and 4 S-wave tomography models. The individual model names and details are shown in Supplementary Figs. 1,2. The dark lines are the average of each panel, which are extracted and shown in the rightmost panels. This procedure is similar to that shown in Fig. 1b and c, but without any vote map analysis.

Figure 5 Vote maps of mantle tomography models. Variable depth vote maps for fast ($>+1\sigma$ from the mean), and slow ($<-1\sigma$ from the mean) mantle for all (a) 4 S-wave and (b) 4 P-wave tomography models (see Methods) considered here. In general, lower mantle vote maps of fast velocity regions reveal subducted slabs, and slow maps reveal plumes and antipodal large low shear wave velocity provinces (LLSVPs). In this map view, the P-wave model vote maps appear less coherent than the S-wave model vote maps in the fast velocity regions of the mid-mantle. Colour maps from⁷¹.

Figure 6 Vertical cross sections through the vote maps. All 4 S-wave models (left) and 4 P-wave models (right) are used for profiles through (a) SE Asia and (b) the Farallon slab regions (vote maps for fast velocities), and (c) the African-Afar large low shear wave velocity province (LLSVP) and plume region (vote maps for slow velocities). Location maps are overlain with palaeo-subduction zones between 0-200 Ma as extracted from a global plate reconstruction⁷³. Panels (a) and (b) identify vertically coherent fast regions that are common to S-wave models in the mid-mantle indicating the presence of subducted slabs

whereas the slab signal is weak amongst P-wave models. This is more clear in the fast rather than (c) slow regions because at higher temperatures the HS-LS crossover shifts to depths at the base of the mantle where the seismic signal is dominated by the LLSVPs, and also occurs over a broader depth range.

Figure 7 Difference maps between P-wave and S-wave models. Difference maps for the fast (left panels) and slow (right panels) vote maps constructed by subtracting the S-wave model votes (constructed with 4 models) from P-wave model votes (constructed with 4 models). Yellow areas indicate high votes (i.e. the identification of robust features) in P-wave models but not S-wave models, darker purple areas indicate high votes for S-wave models relative to P-wave models, and central colours indicate regions of mutual agreement.

Figure 1

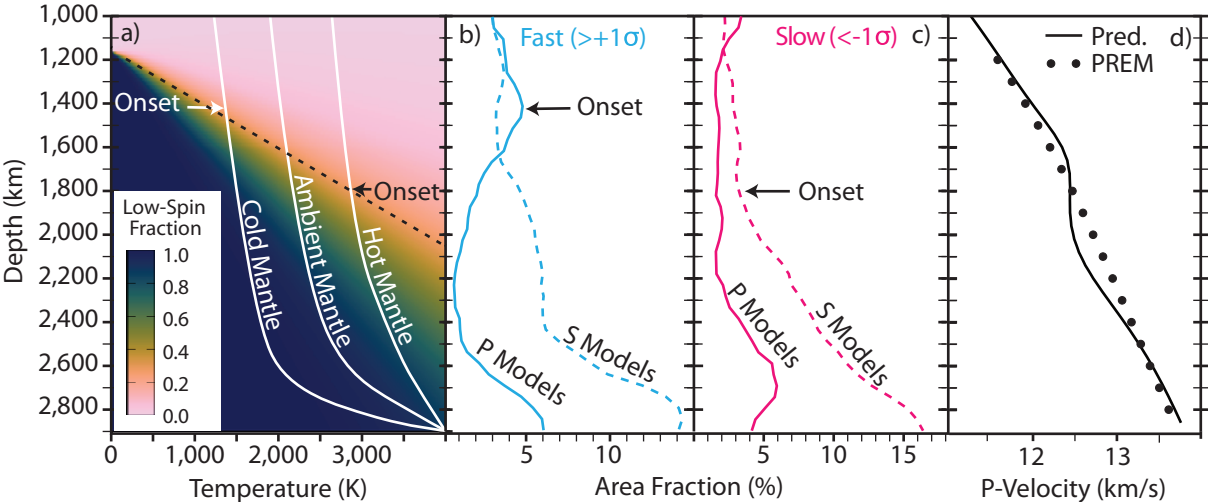


Figure 2

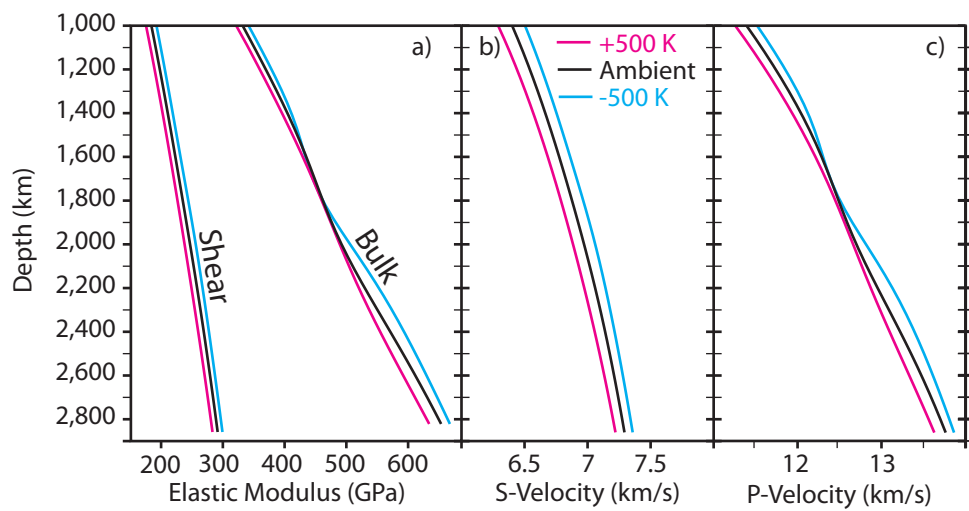


Figure 3

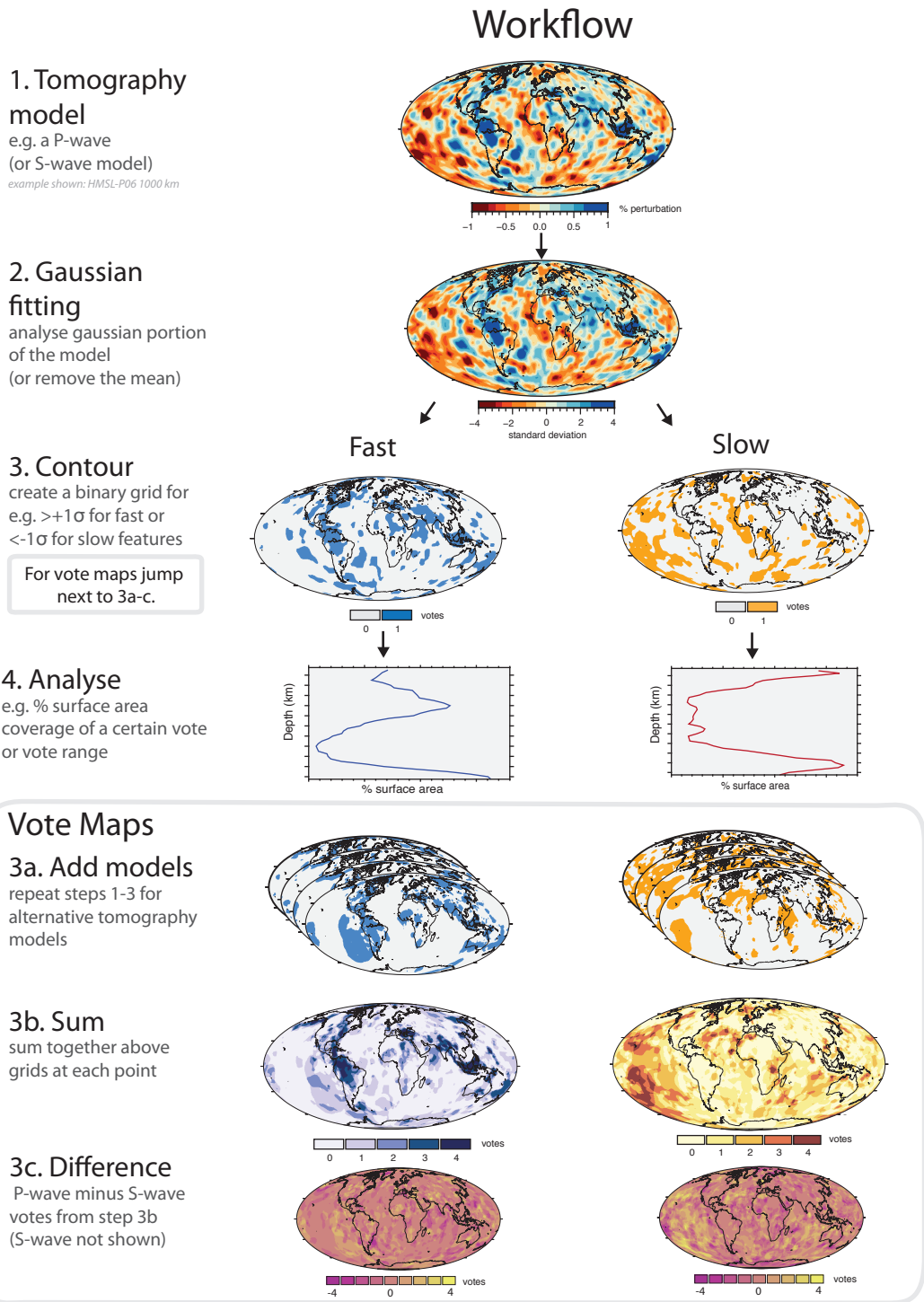
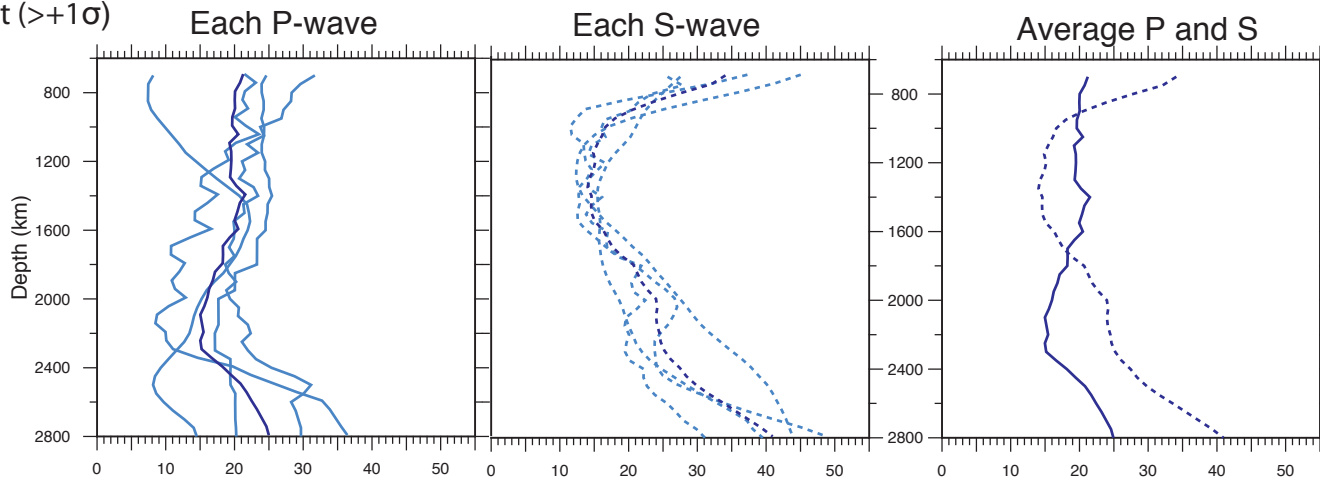
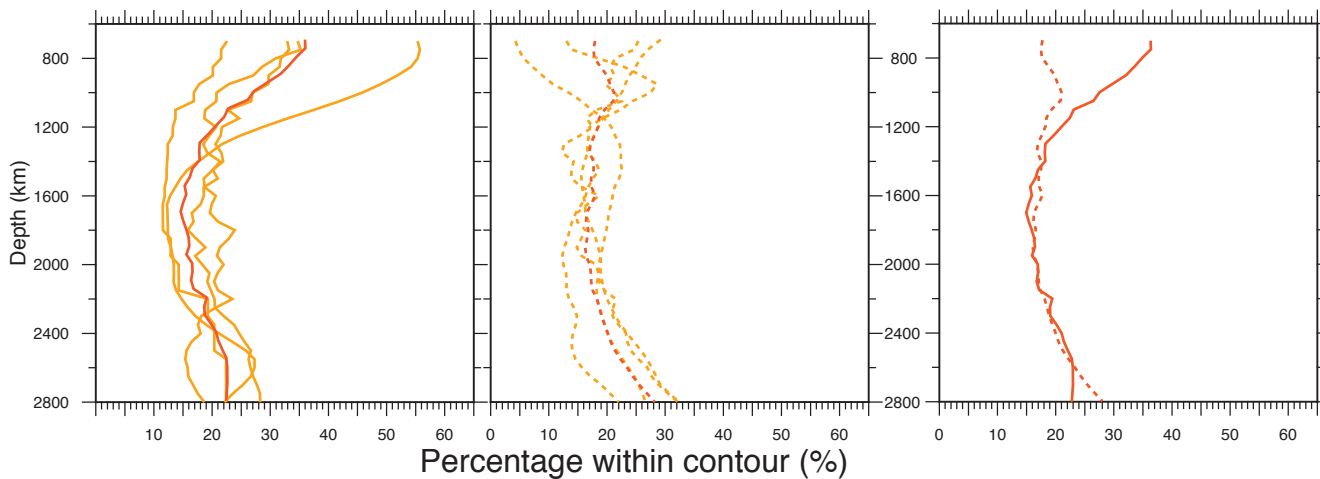


Figure 4

a. Fast ($>+1\sigma$)



b. Slow ($<-1\sigma$)



a.

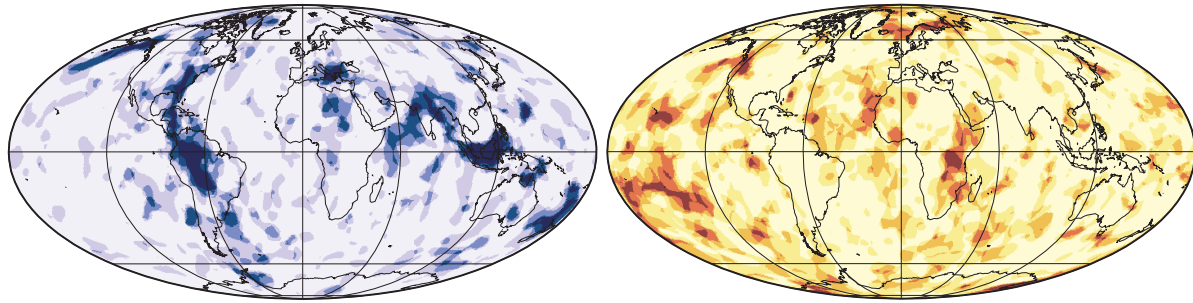
Figure 5

S-wave tomography models

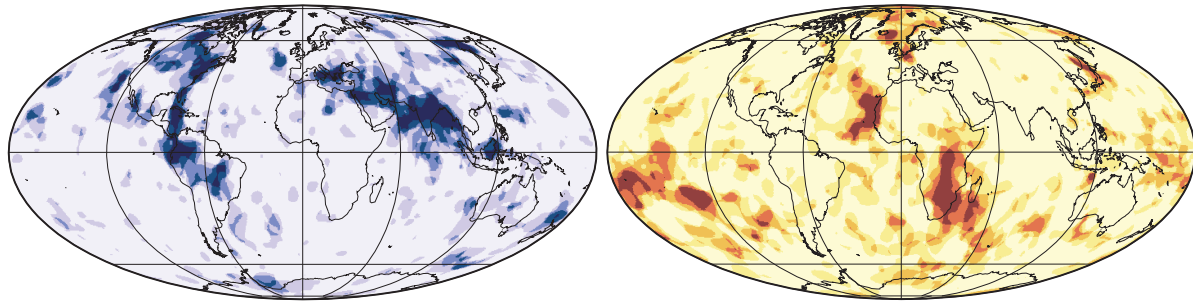
Fast anomalies ($>+1\sigma$)

Slow anomalies ($<-1\sigma$)

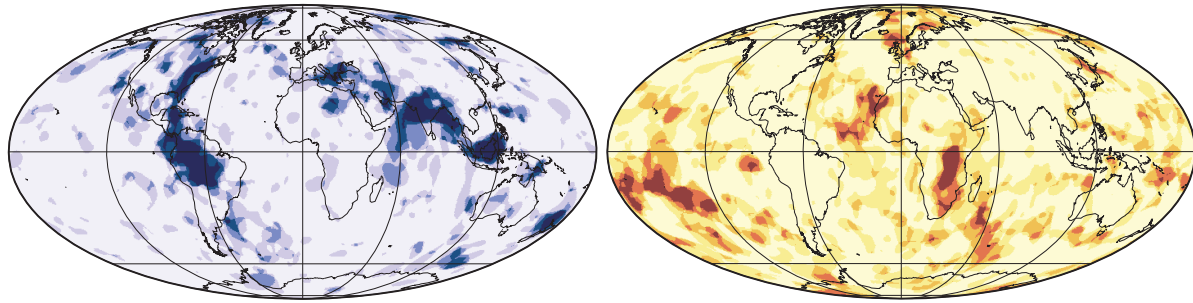
1000 km



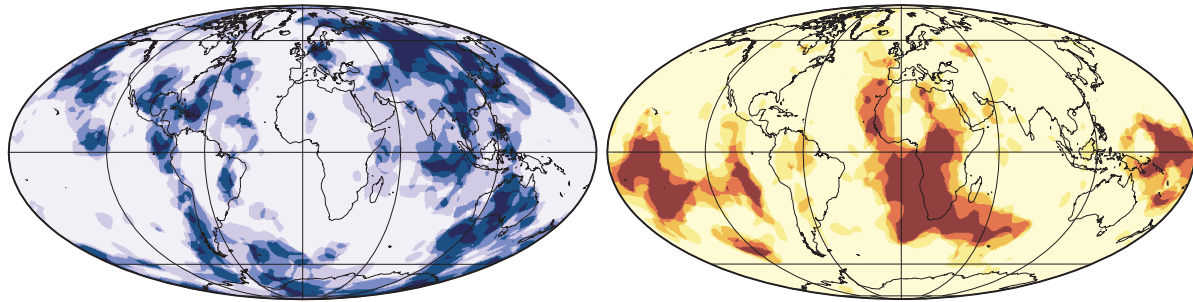
1400 km



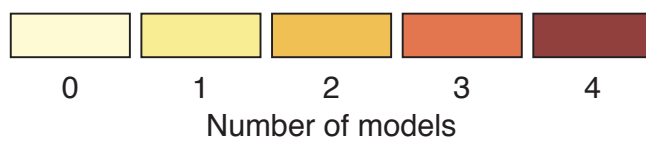
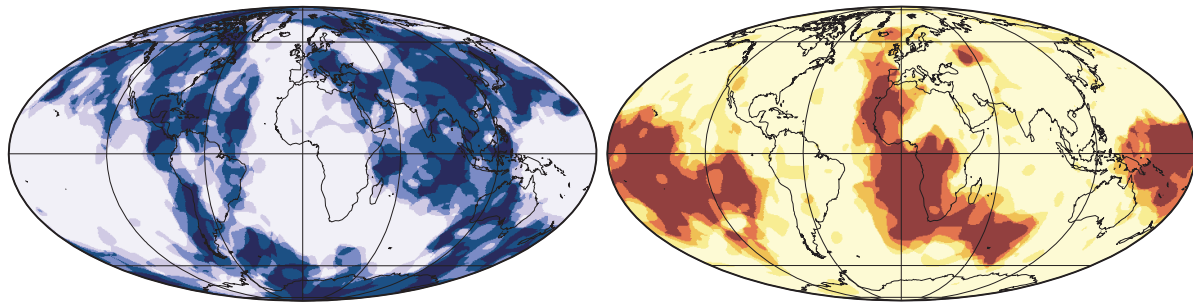
2000 km



2400 km



2800 km



b.

P-wave tomography models

Fast anomalies ($>+1\sigma$)

Slow anomalies ($<-1\sigma$)

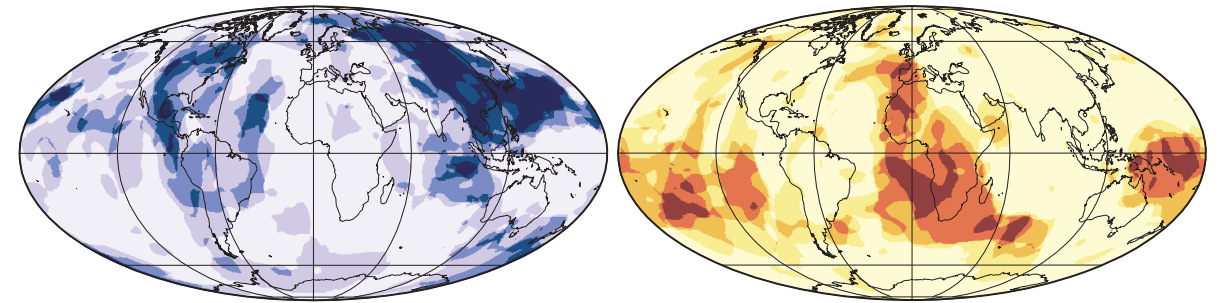
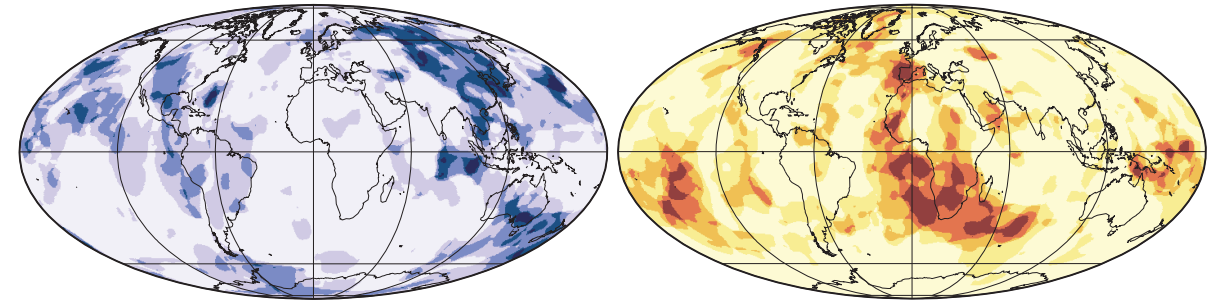
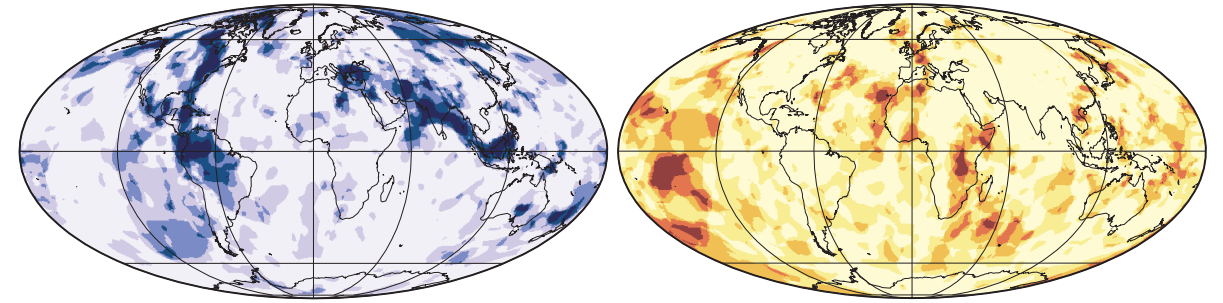
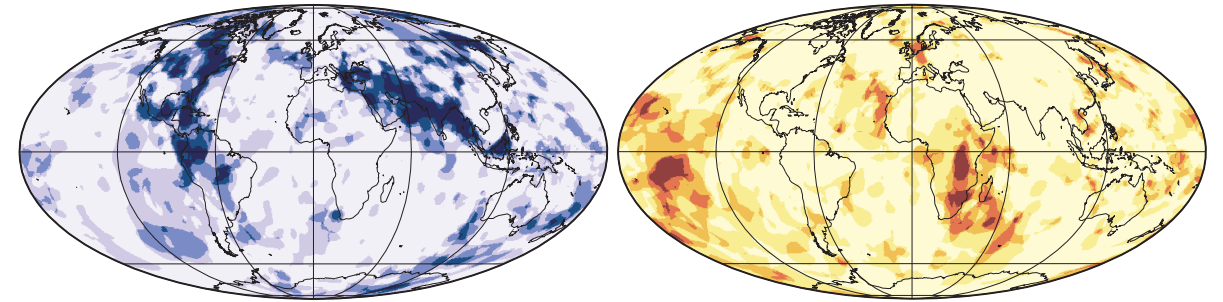
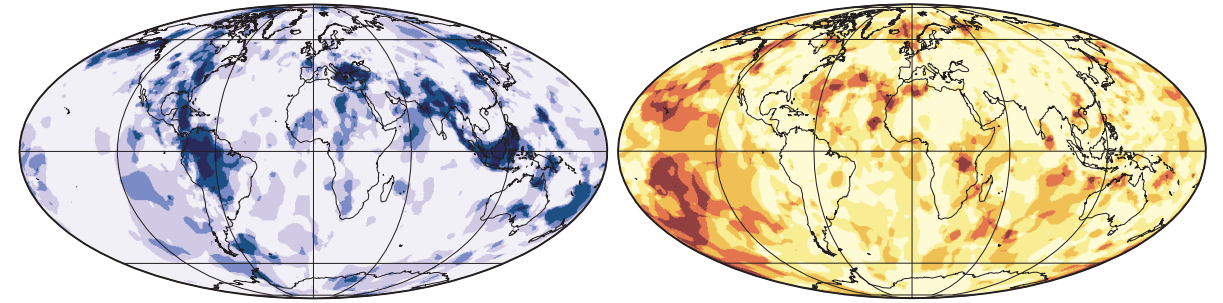
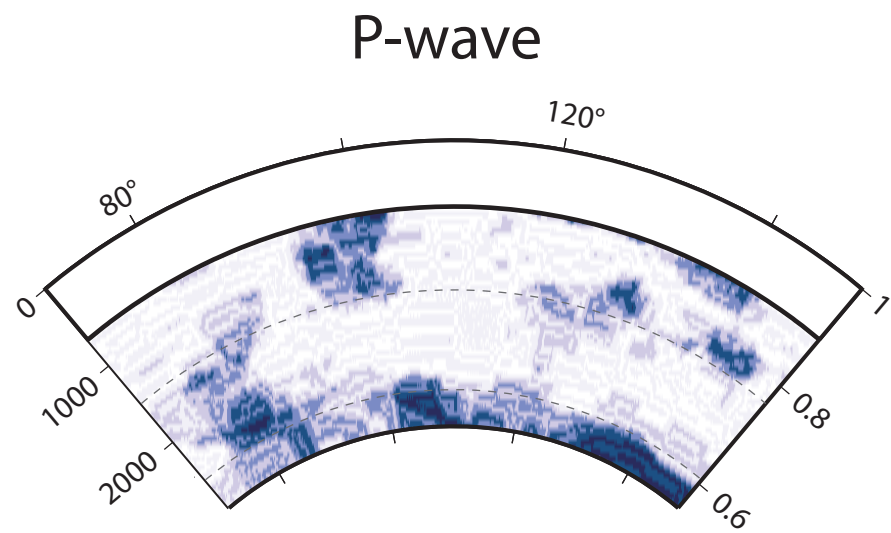
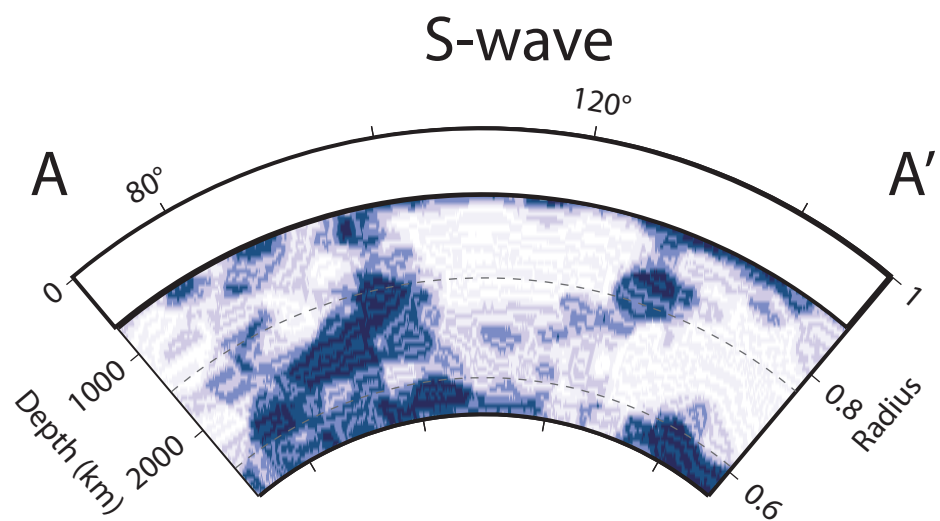
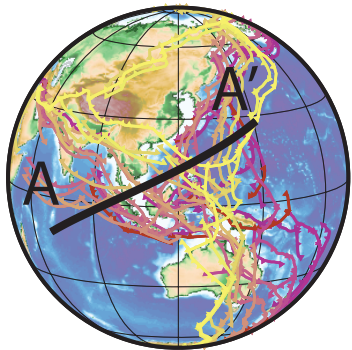
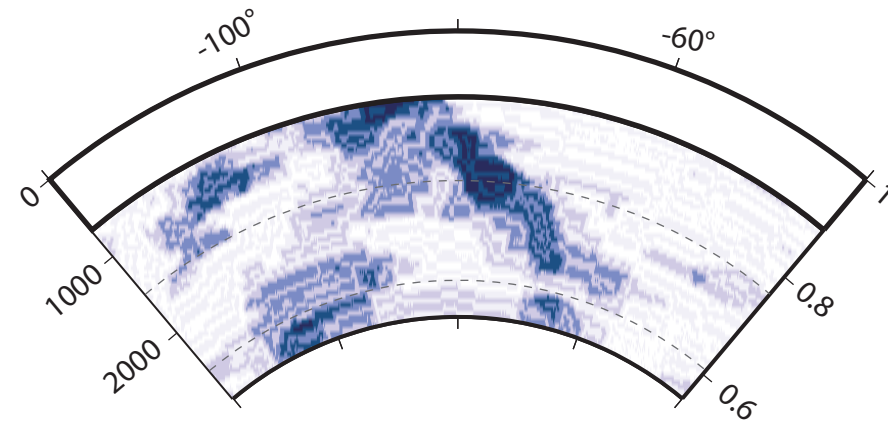
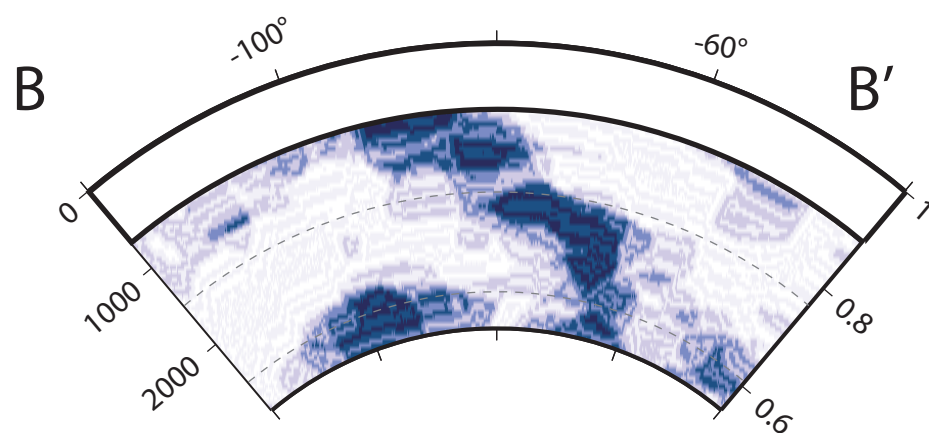
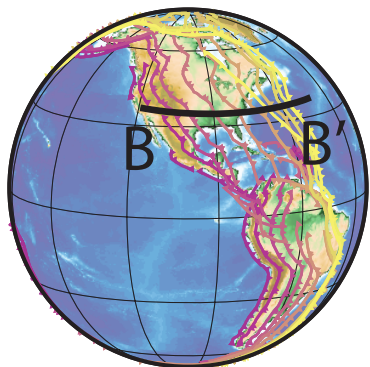


Figure 6

a.



b.



c.

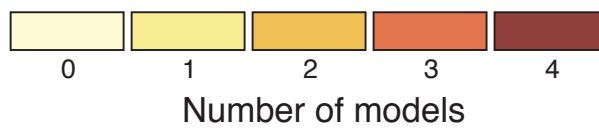
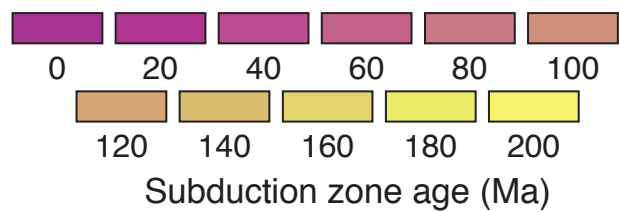
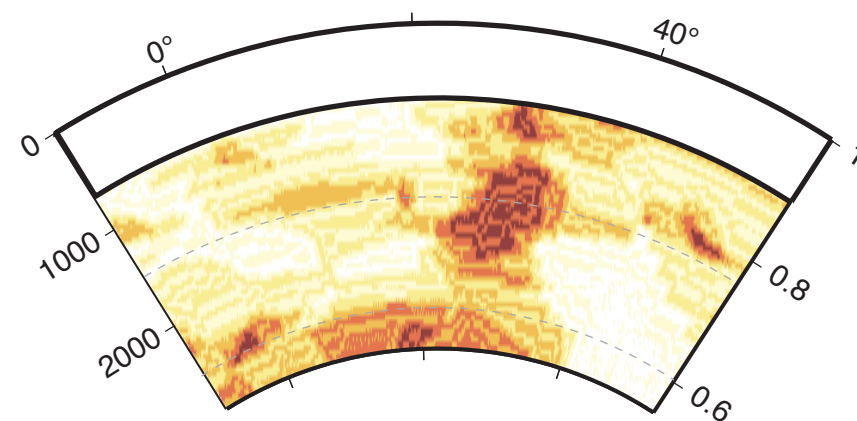
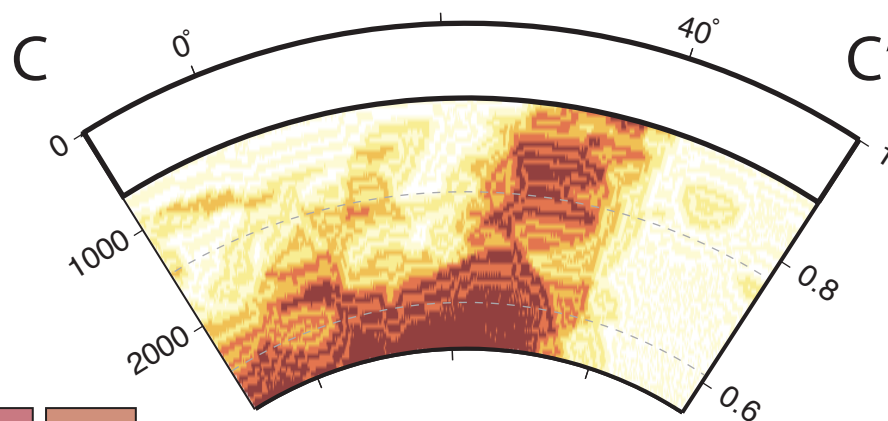
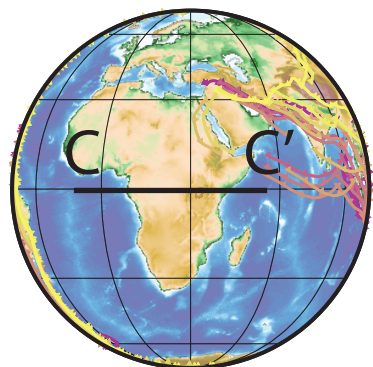
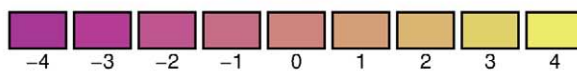
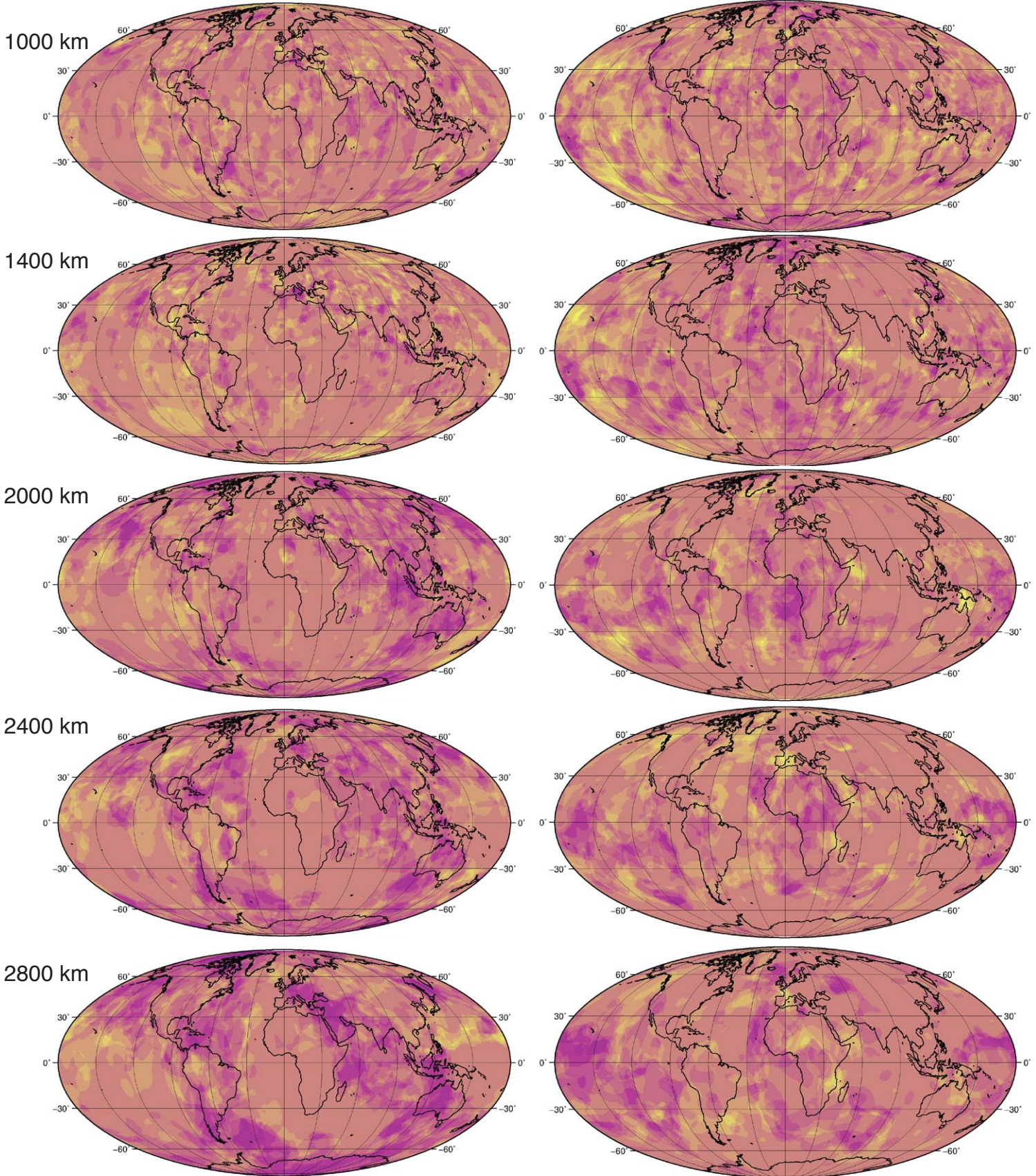


Figure 7

Difference (P-wave minus S-wave votes)

Fast anomalies ($>+1\sigma$)

Slow anomalies ($<-1\sigma$)



Number of votes (V_p minus V_s)

Supplementary Information: Seismological Expression of the Iron Spin Crossover in Ferropericlase in the Earth's Lower Mantle

Grace E. Shephard*¹, Christine Houser², John W. Hernlund², Juan J. Valencia-Cardona³, Reidar G. Trønnes^{1,4}, Renata M. Wentzcovitch^{2,5,6}

1 Centre for Earth Evolution and Dynamics (CEED), Department of Geosciences, University of Oslo, Norway **2** Earth-Life Science Institute, Tokyo Institute of Technology, Tokyo, Japan **3** Department of Chemical Engineering and Material Science, University of Minnesota, Twin Cities, USA **4** Natural History Museum, University of Oslo, Norway **5** Department of Earth and Environmental Sciences, Columbia University, Lamont-Doherty Earth Observatory, Palisades, USA **6** Department of Applied Physics and Applied Mathematics, Columbia University, New York City, USA

Supplementary Figures

Supplementary Figure 1 Calculated shear and compressional velocities using the *ab initio* technique described in Methods section for harzburgite (top) and an Fp-free model composition with 94 and 6 mol% of Bm and Ca-perovskite, respectively (bottom). The *ab initio* calculations were performed for each composition with the self consistent geotherm anchored at 1873 K at the top of the lower mantle (black) along with the same calculation anchored at 500 K below (blue) and a 500 K above (magenta). The properties of individual minerals were calculated using an ideal

solid solution formalism, where the end-members were the Mg-compound and a (Mg,Fe) solid solution with Mg = 0.875 and Fe = 0.125 for bridgmanite ¹ and Mg = 0.8125 and Fe = 0.1875 for ferropericlase ². Aggregate elastic properties were obtained using the Voigt-Reuss-Hill average for the Fp-free mantle model composition, consisting of 94 wt.% bridgmanite and 6 wt.% calcium perovskite and Fp-rich harzburgite consisting of 75 wt.% bridgmanite, 23 wt.% ferropericlase, and 2 wt.% calcium perovskite.

Supplementary Figure 2 Surface area coverage for individual models and for variable sigma contours, for fast anomalies. Area fraction of fast ($>+0.75$, $>+1$, $>+1.25 \sigma$) anomalies as a function of depth for the 8 tomography models individually. This is similar to Fig. 1b and 4a (and Supplementary Fig. 5 for HMSL³), but presented here for the individual tomography models (4 P-wave and 4 S-wave) prior to being summed into the vote map. There is high variability between and within the individual tomography models, including the joint HMSL models. While a decorrelation between P- and S-wave models is apparent between some model combinations, it is not in others, which is why a single pair of tomography models in isolation may not render a robust signal of the spin transition. Other features in these models, such as the oscillatory behaviour in HMSL, are not well understood and can also distract from the broader trends in P-wave and S-wave velocity.

Supplementary Figure 3 Surface area coverage for individual models and for variable sigma contours, for slow anomalies. Area fractions of slow (<-0.75 , <-1 , $<-1.25 \sigma$) anomalies as a function of depth for the 8 tomography models. Similar to Fig. 1c, but here presented for the individual

tomography models (4 P-wave and 4 S-wave) prior to being summed into the vote map. As with the fast anomalies (Supplementary Figure 2), there is high variability between the tomography models. Other features in these models, such as the oscillatory behaviour in HMSL, are not well understood and can also distract from the broader trends in P-wave and S-wave velocity.

Supplementary Figure 4 A graphical example figure of the contouring procedure for fast anomalies at 1000 km depth. This step occurs before the models are added into vote maps and are equivalent to what is shown in Supplementary Figures 2-3, and Figure 3 Steps 1-3. Each of the 8 tomography models are shown in their original format (panel a) and after the gaussian fitting is applied to 1000-2200 km depth (panel b; See Supplementary Figures 10 and 11 for details). The models are contoured for values equal to or higher than $+0.75$, $+1$, $+1.25 \sigma$ anomalies for the P-wave models (panels c, d, e) and S-wave models (panels f, g, h), respectively. The fast vote maps in the main manuscript were constructed from the $>+1$ sigma vote maps. Shephard et al. (2017)⁴ presents further details of the vote map methodology.

Supplementary Figure 5 The influence of using fewer tomography models. Area coverage as a function of depth for the sequential addition of tomography models used in this study. P-wave models (solid) and S-wave models (dashed), top panels (a) show fast anomalies, and bottom (b) panels show slow anomalies. Models used are listed within each panel (the HMSL profiles (1 model) are the same as shown in Supplementary Figures 2 and 3). There is an apparent decorrelation of P-wave and S-wave profiles in all combinations. However, the signal becomes more apparent when the models are summed into the vote maps, which identify the most common fea-

tures between tomography models.

Supplementary Figure 6 Comparison of the vote map procedure for alternative combinations using 3 of the 4 alternative tomography models used in the manuscript, for V_p (solid) and V_s (dashed). The combination models are listed within each panel. The surface area is the coverage for the (maximum) 3 votes, and is complementary to Figure 1b and 1c which shows the maximum 4 votes. Fast velocities are shown in the top panels (a) and slow velocities in the lower panels (b). While there is some variability between the combinations, the observed decorrelation between P- and S-wave velocity models is consistent at 1400 km for fast velocities and 1800 km for the slow velocities. This suggests that, regardless of which three models are used (conversely, the one model which is excluded), the effects of the iron spin cross-over in ferropericlasite can be observed.

Supplementary Figure 7 Comparison of depth-dependent changes in surface area for alternative vote combinations, V_p (solid) and V_s (dashed). In Figure 1, only the maximum vote of 4 was shown. The vote counts are listed in the inset panel. Fast velocities are shown in the top panels (a) and slow velocities in the lower panels (b). For the combination of 4 and 4+3 votes (and 4+3+2 for the fast anomalies), the decorrelation signal is very similar. However, when 2 and 1 votes are also added the signal becomes more complicated; this is due to the potential inclusion of noise/artefacts which may not be robust features (because only one model captured it; see Shephard et al. (2017) for further details). Nonetheless, the robustness of the signal suggests that the effects of the iron spin cross-over can be observed.

Supplementary Figure 8 The change in the seismic velocities using constant versus depth-

dependent partitioning of iron between Br and Fp, K_D . Panel (a): Depth-dependent K_D^5 curve (dashed line) and the constant 0.5 value (solid line) used in the main text. Panels (b and c): Shear and compressional velocities for the depth-dependent K_D^5 case (dashed lines) and the constant value 0.5 case (solid lines, same as Figure 2). A higher proportion of Fe in the ferropericlasite (lower K_D) may increase the crossover pressure⁶. We find that Fe in ferropericlasite remains below the 25% threshold for observing substantial increases in the crossover transition pressure⁷ for the depth-dependent K_D case. Thus, depth-dependent K_D does not have a significant influence on the crossover depth/pressure range over which we observe the anomalous signal in compressional velocity in the tomographic models.

Supplementary Figure 9 The self-consistent geotherms for pyrolite. These are calculated by setting the starting temperature of the calculation at the top of the lower mantle to 1373 K (blue, the -500 K case), 1873 K (black, the average case), and 2373 K (red, the +500 K case) for the elastic moduli and velocity profiles plotted in Figure 2.

Supplementary Figure 10 Analysis of velocity-frequency distributions of a variety of tomographic models reveals that they exhibit significant differences that may confound inter-model comparisons (Hernlund and Houser, 2008). These differences can be categorized via scale/amplitude (caused by variability in tomographic model data and construction), shift/alignment (caused by reference to different 1D seismic velocity models) and the shape of the distributions (related to variations in the distribution that remain even after accounting for relative shifting of the reference baseline and scaling of amplitudes). There is a large difference in the models between the depth

range of 1000-2200 km (see also Hernlund and Houser, 2008). In order to account for this we analyse the Gaussian portion of the models at each depth, derived from this depth range and applied to all mantle depths. See also Supplementary Figure 11.).

Supplementary Figure 11 Panels a and b reveal the depth-dependent mean and standard deviation for each of the 8 individual models used in this study, respectively, before any gaussian fitting is applied. The recalculated standard deviations after the fitting (see Extended Figure 10) are shown in panels c, the black lines are the average of the 4 models and are used in panel d. Panel d shows the ratio of the (averaged) standard deviation of the S wave models (from panel c) as compared to the P wave models. There is an increase in the ration of RS/P between the depths of 1200-2000 km depth. In summary, the gaussian fitting procedure does not affect the relative variation of seismic velocities in the models, it only serves to bring them into alignment and forces their core velocity variations to exhibit similar amplitudes.

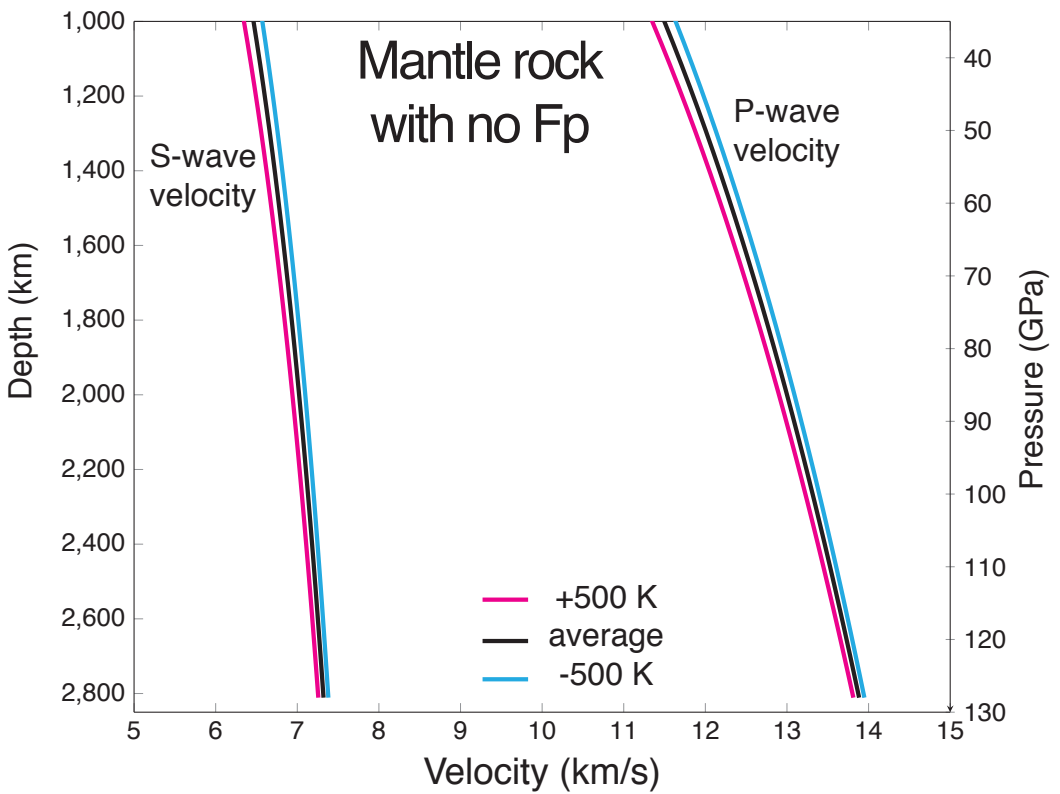
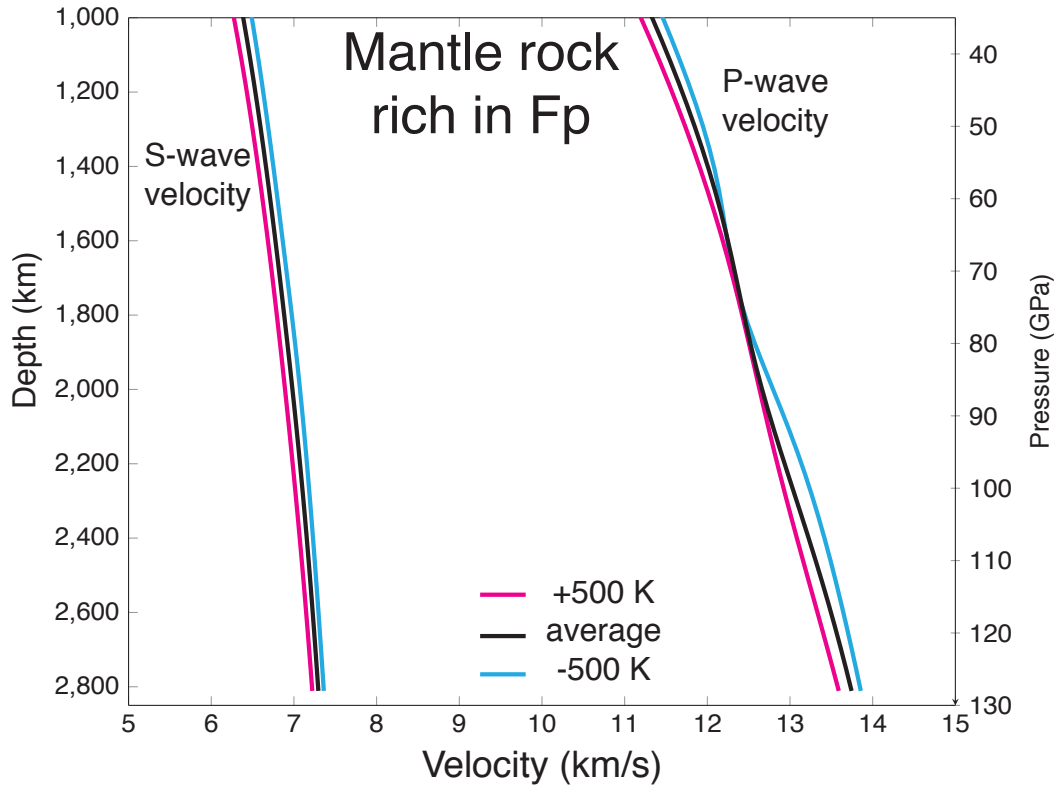
Supplementary Figure 12 In addition to the eight models used in the paper, depth-dependent change in surface areas for the joint tomography models of SP12RTS⁸ and TX2019⁹ are also included for reference. The trend between P- and S-wave models is somewhat variable between the individual model pairs of SP12RTS, TX2019, (as for HMSL, Supplementary Figure 5) but do hint at a mid-mantle decorrelation related to the spin crossover.

1. Shukla, G. *et al.* Thermoelasticity of Fe²⁺-bearing bridgmanite. *Geophys. Res. Lett.* **42**, 1741–1749 (2015).

2. Wu, Z., Justo, J. & Wentzcovitch, R. Elastic anomalies in a spin-crossover system: Ferropericlase at lower mantle conditions. *Phys. Rev. Lett.* **110**, 228501 (2013).
3. Houser, C., Masters, G., Shearer, P. & Laske, G. Shear and compressional velocity models of the mantle from cluster analysis of long-period waveforms. *Geophys. J. Int.* **174**, 195–212 (2008).
4. Shephard, G., Matthews, K., Hosseini, K. & Domeier, M. On the consistency of seismically imaged lower mantle slabs. *Science Reports* **7**: **10976** (2017).
5. Piet, H. *et al.* Spin and valence dependence of iron partitioning in Earth's deep mantle. *Proc. Nat. Acad. Sci.* **113** (40), 11,127–11,130 (2016).
6. Lin, J.-F., Speziale, S., Mao, Z. & Marquardt, H. Effects of the electronic spin transitions of iron in lower mantle minerals: Implications for deep mantle geophysics and geochemistry. *Reviews of Geophysics* **51**, 244–275 (2013).
7. Persson, K., Bengtson, A., Ceder, G. & Morgan, D. Ab initio study of the composition dependence of the pressure-induced spin transition in the $(\text{Mg}_{1-x}\text{Fe}_x)\text{O}$ system. *Geophys. Res. Lett.* **33**, L16306 (2006).
8. Koelemeijer, P., Ritsema, J., Deuss, A. & van Heijst, H.-J. SP12RTS: A degree-12 model of shear- and compressional-wave velocity for Earth's mantle. *Geophysical Journal International* **204**, 1024–1039 (2016).

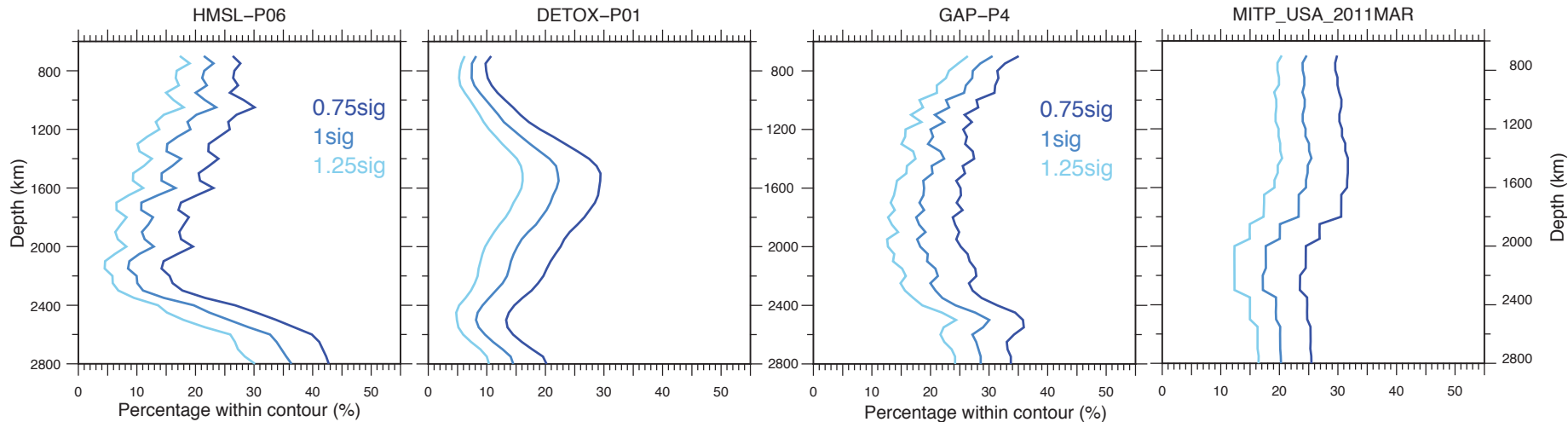
9. Lu, C., Grand, S. P., Lai, H. & Garnero, E. J. TX2019slab: A new P and S tomography model incorporating subducting slabs. *Journal of Geophysical Research: Solid Earth* **124**, 11549–11567 (2019).

Supplementary Figure 1

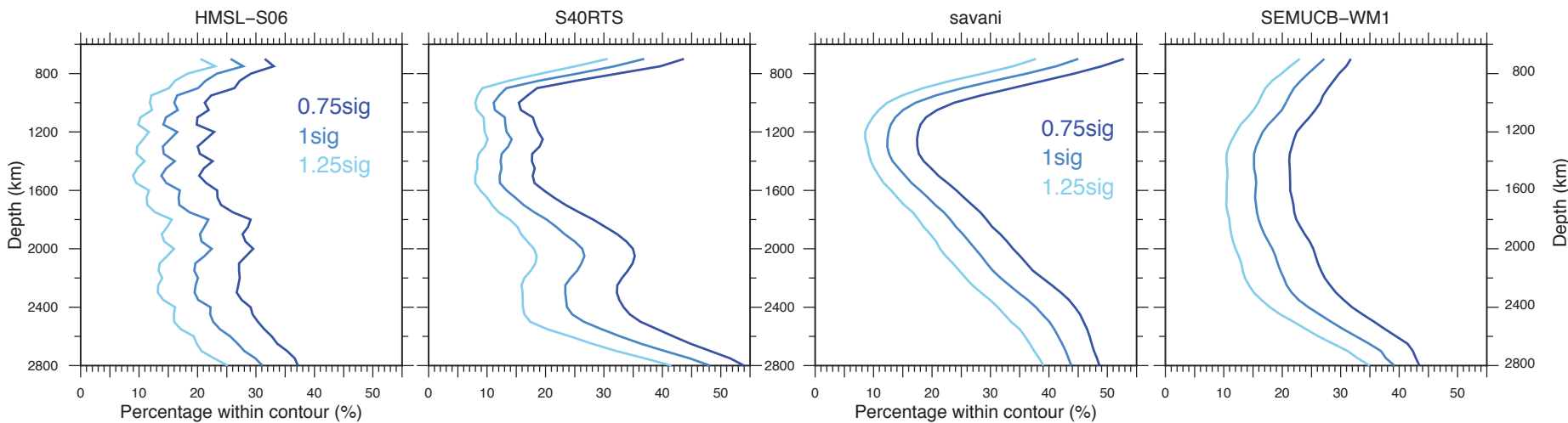


P-wave tomography models (fast anomalies)

Supplementary Figure 2



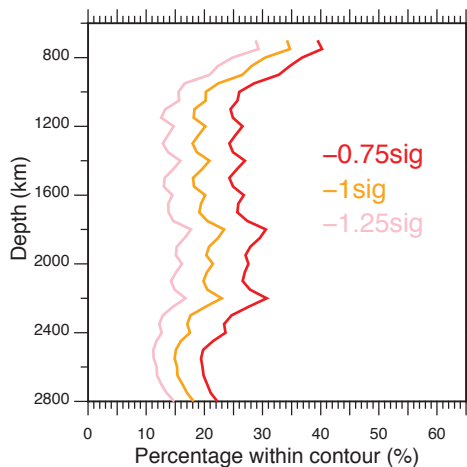
S-wave tomography models (fast anomalies)



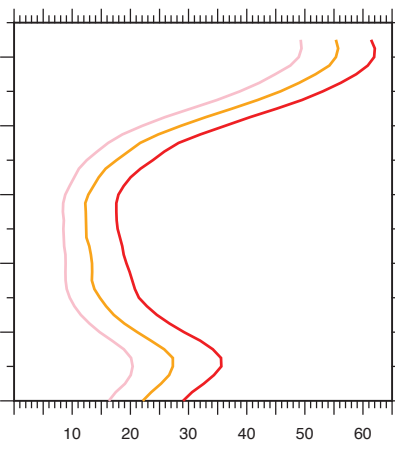
P-wave tomography models (slow anomalies)

Supplementary Figure 3

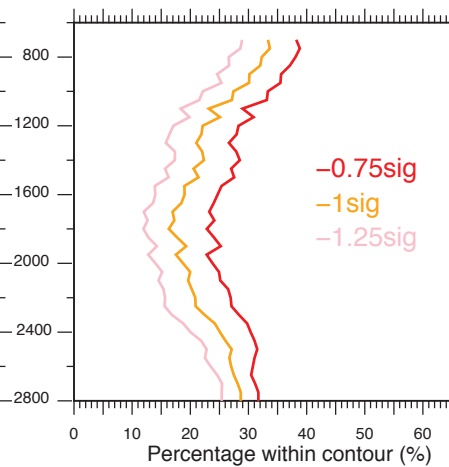
HMSL-P06



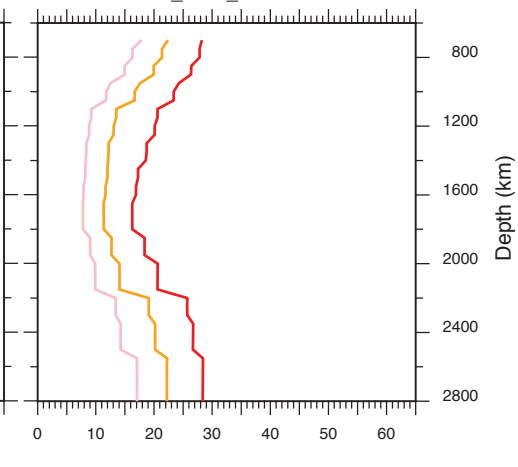
DETOX-P01



GAP-P4

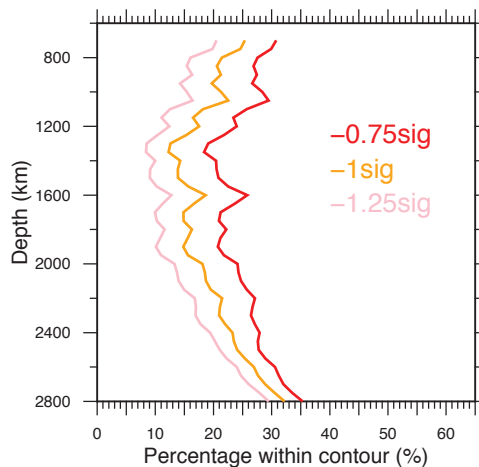


MITP_USA_2011MAR

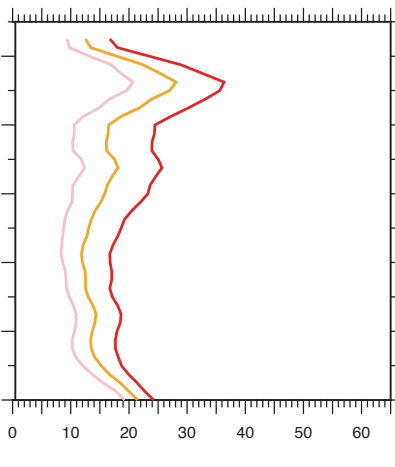


S-wave tomography models (slow anomalies)

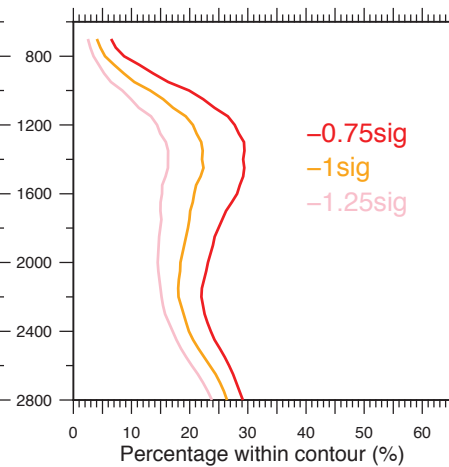
HMSL-S06



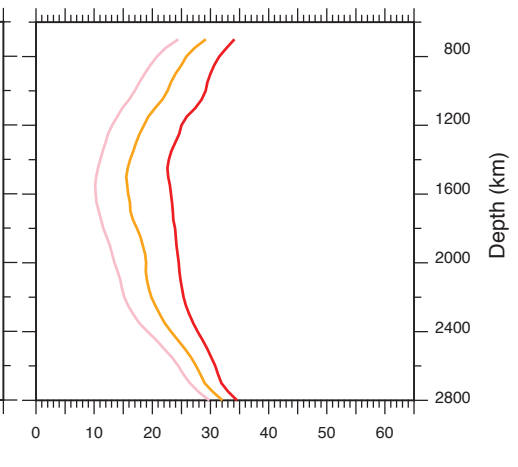
S40RTS



savani

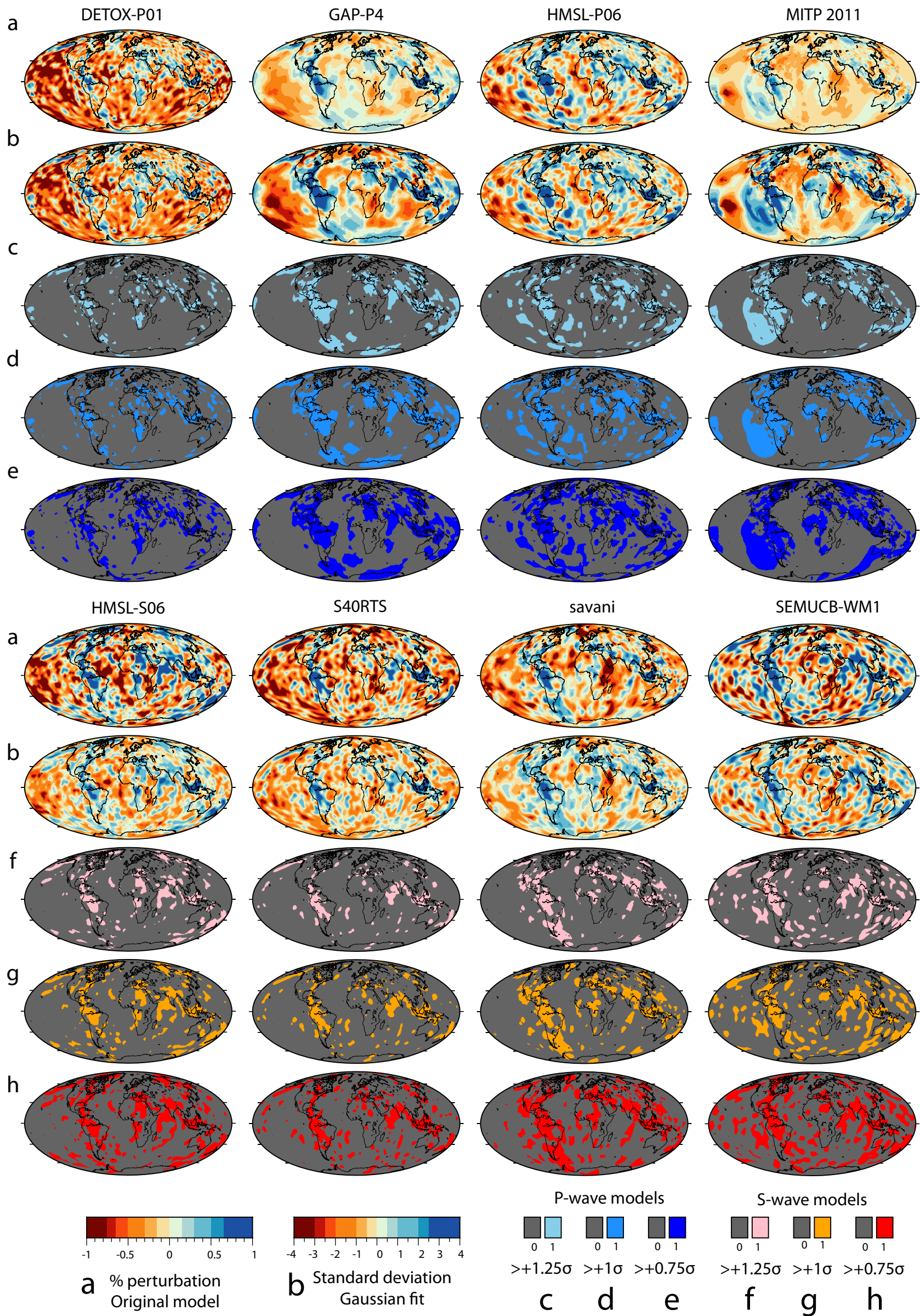


SEMUCB-WM1



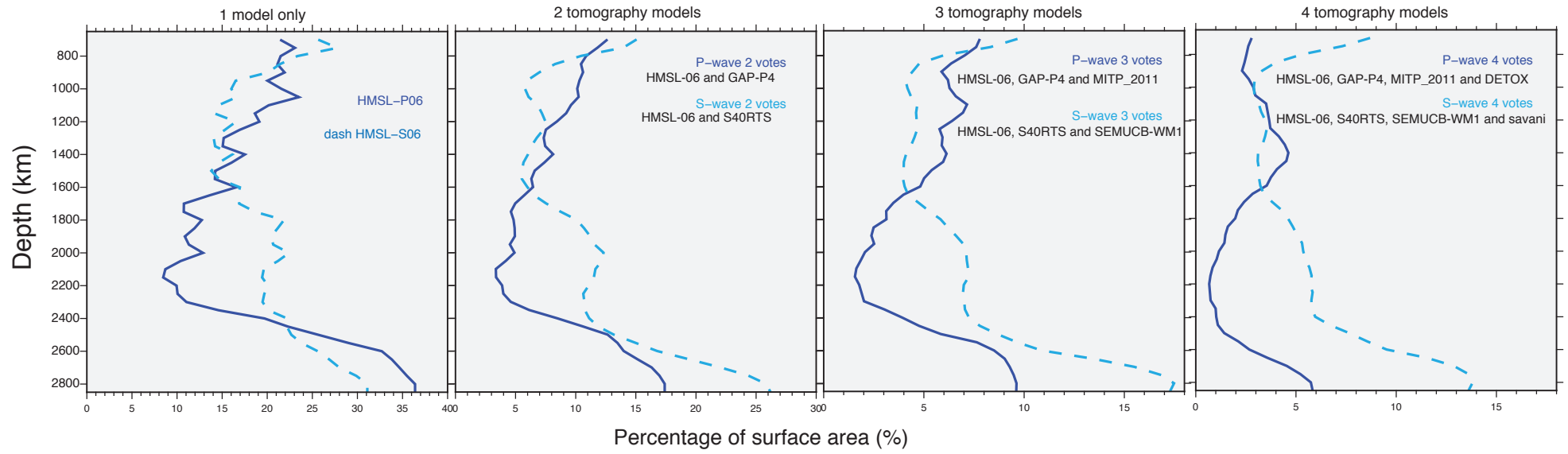
Fast anomalies at 1000 km depth

Supplementary Figure 4



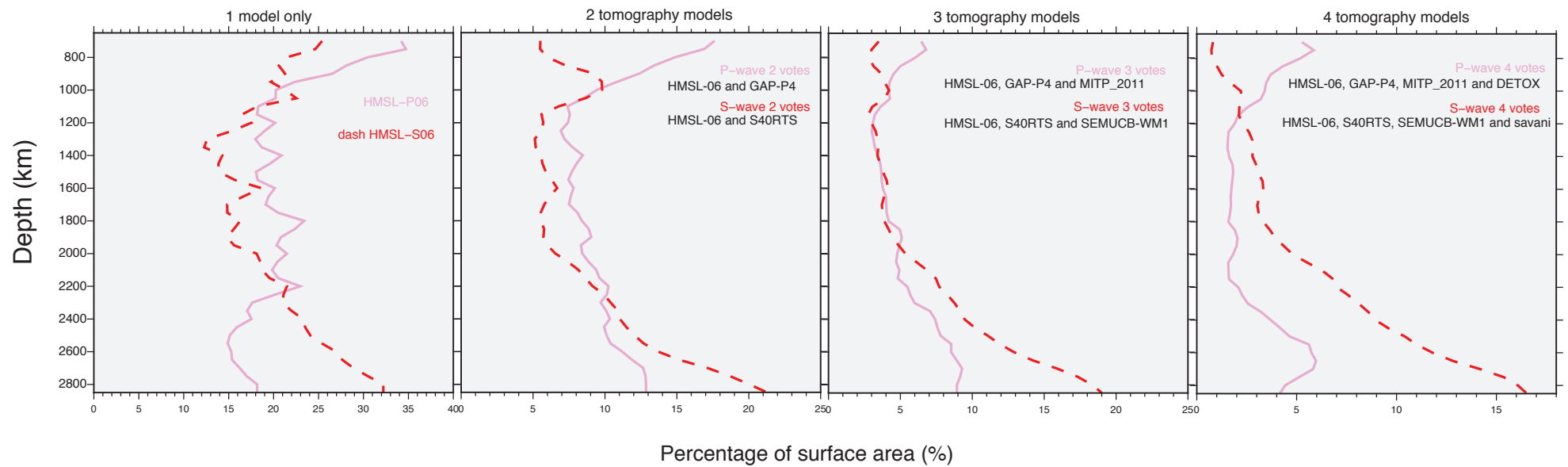
a. Supplementary Figure 5

Fast anomalies ($>+1\sigma$)



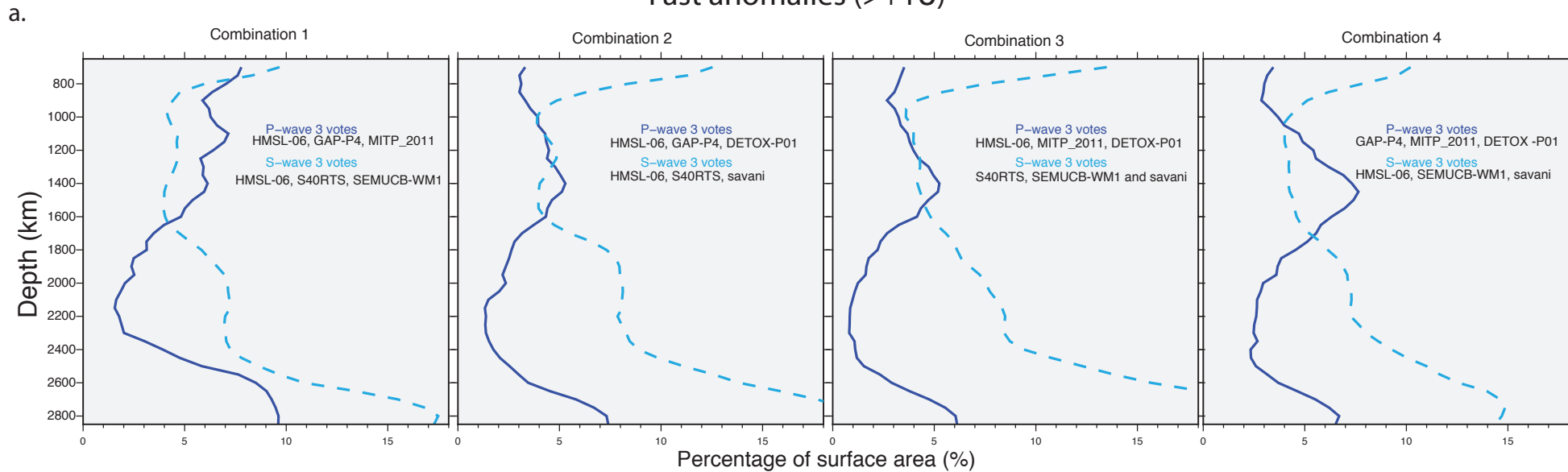
b.

Slow anomalies ($<-1\sigma$)

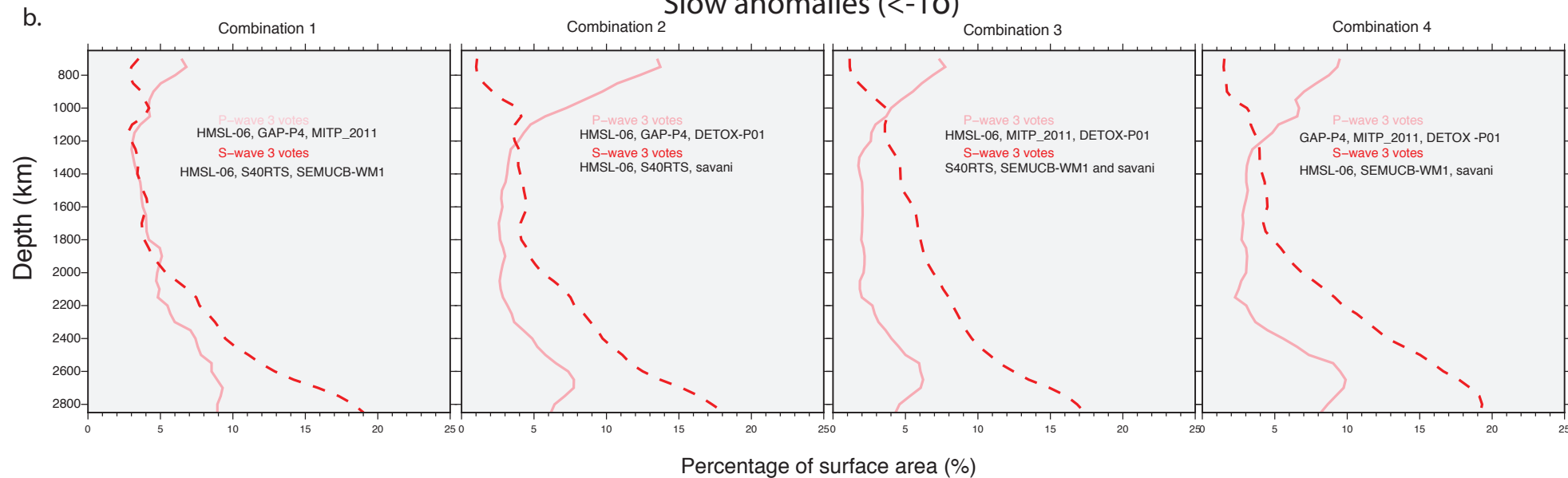


Supplementary Figure 6

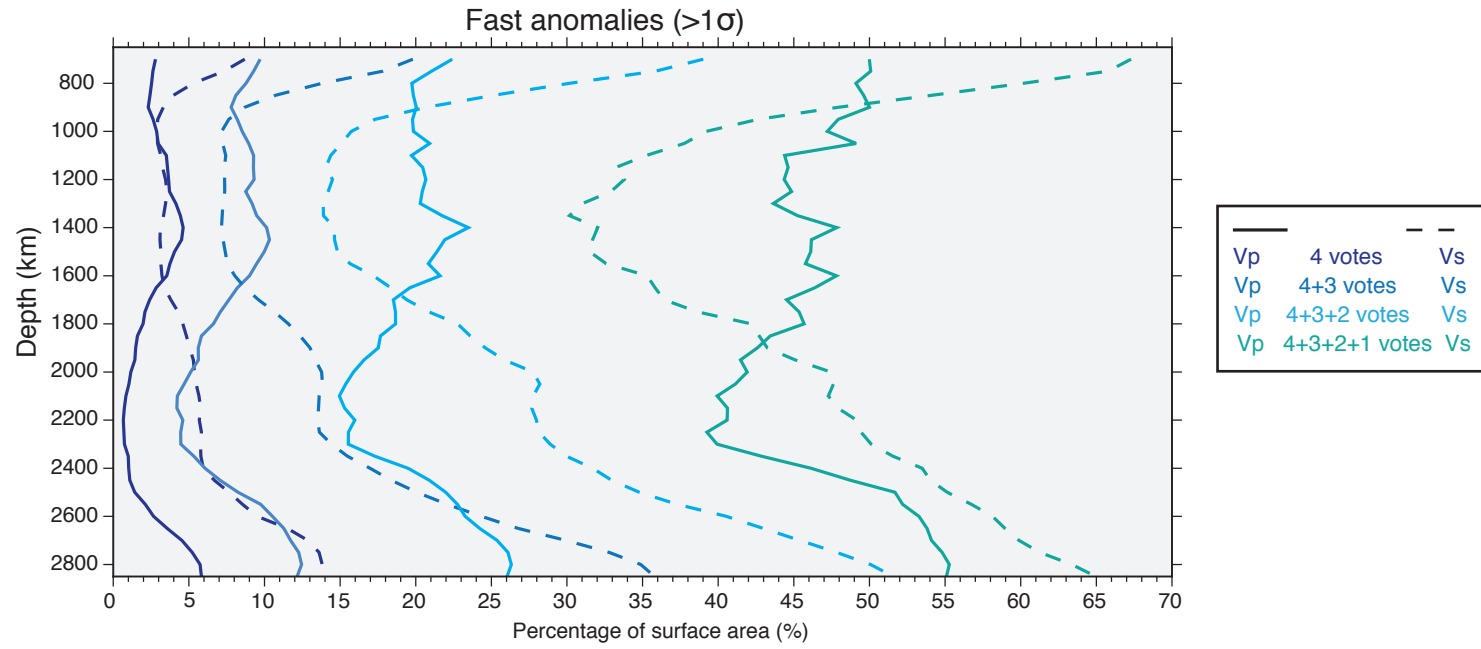
Fast anomalies ($>+1\sigma$)



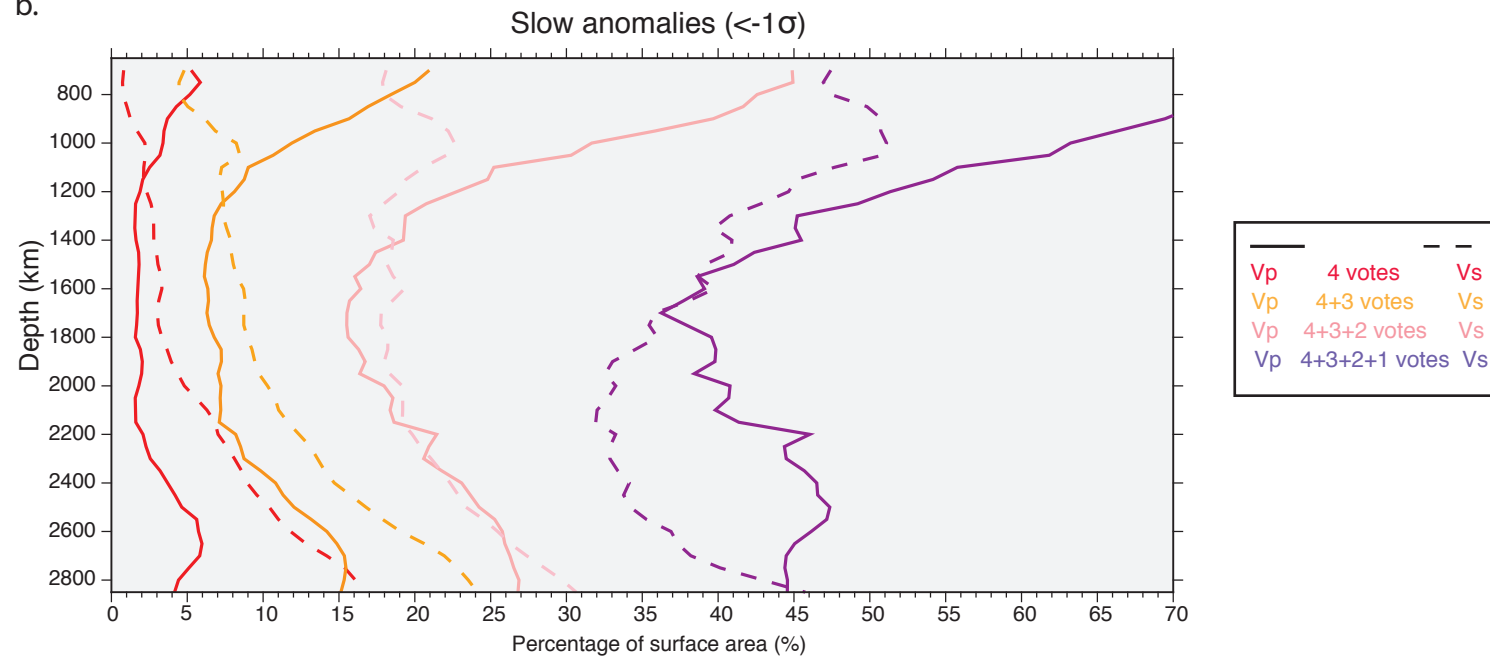
Slow anomalies ($<-1\sigma$)



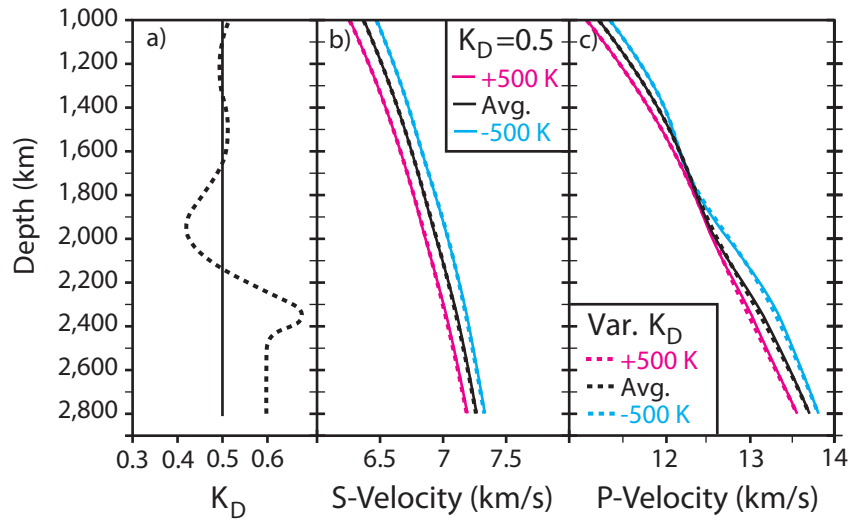
a. Supplementary Figure 7



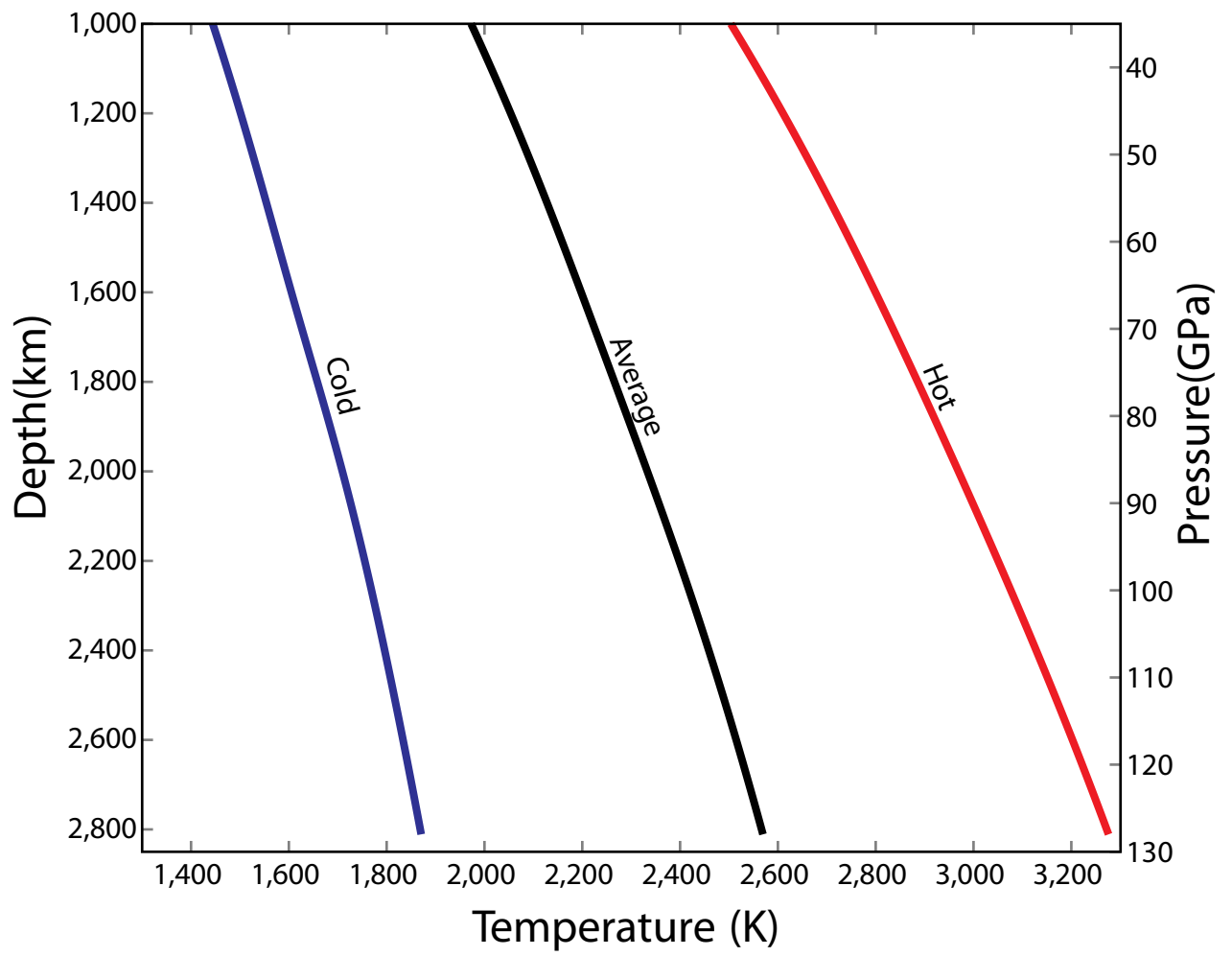
b.



Supplementary Figure 8

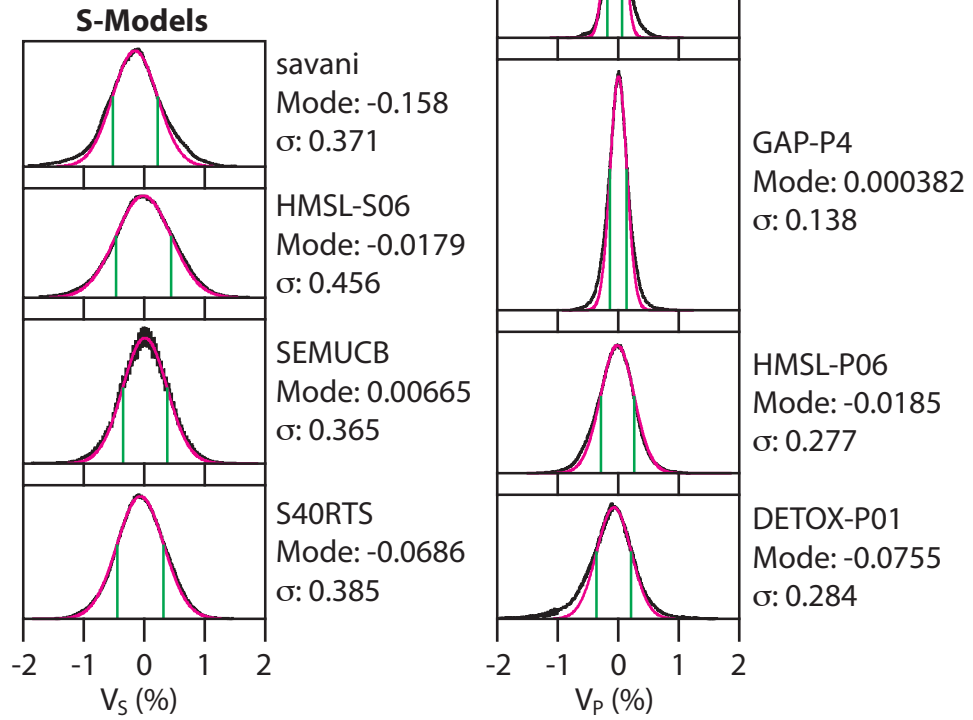


Supplementary Figure 9

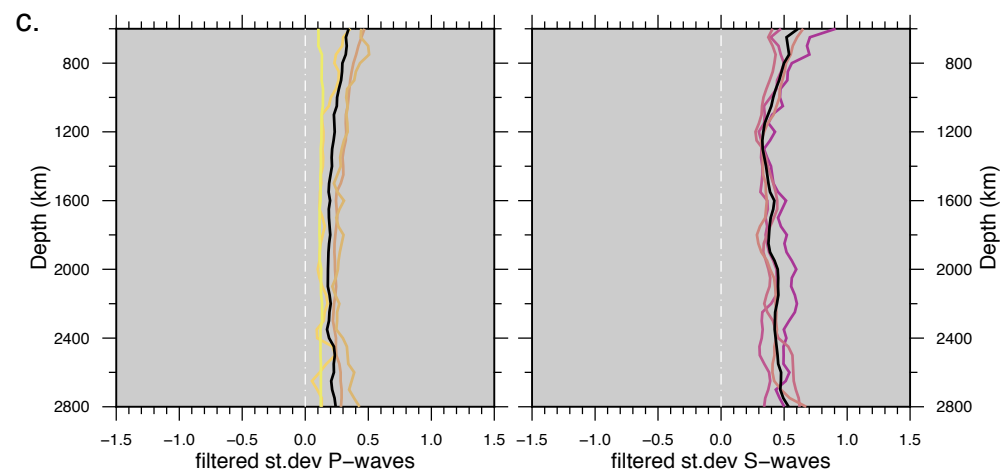
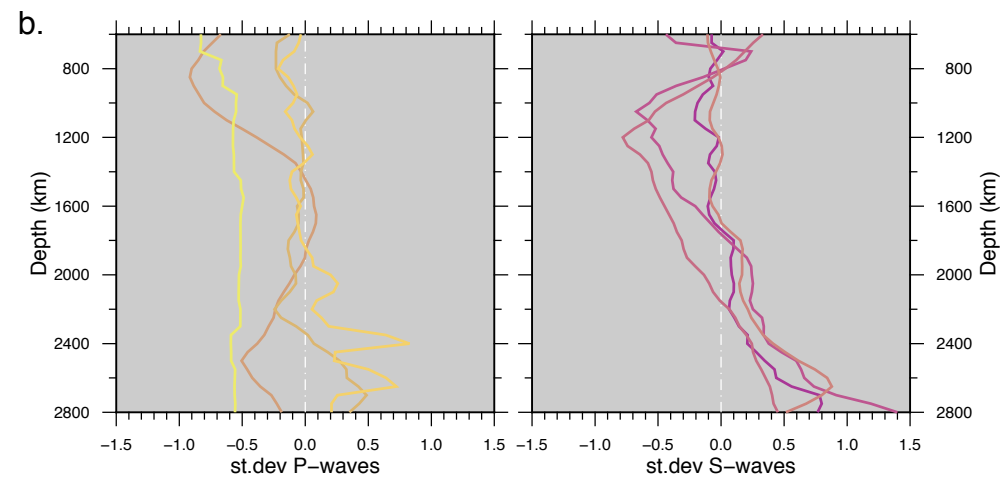
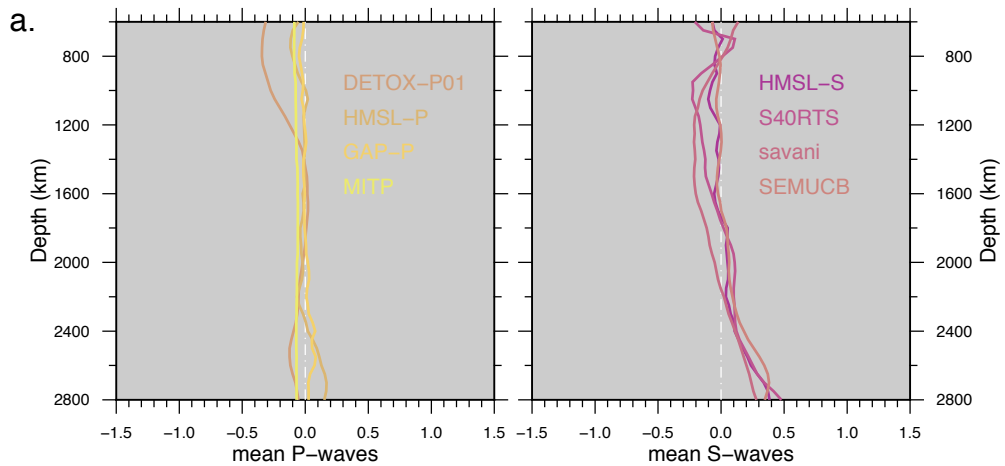


Supplementary Figure 10

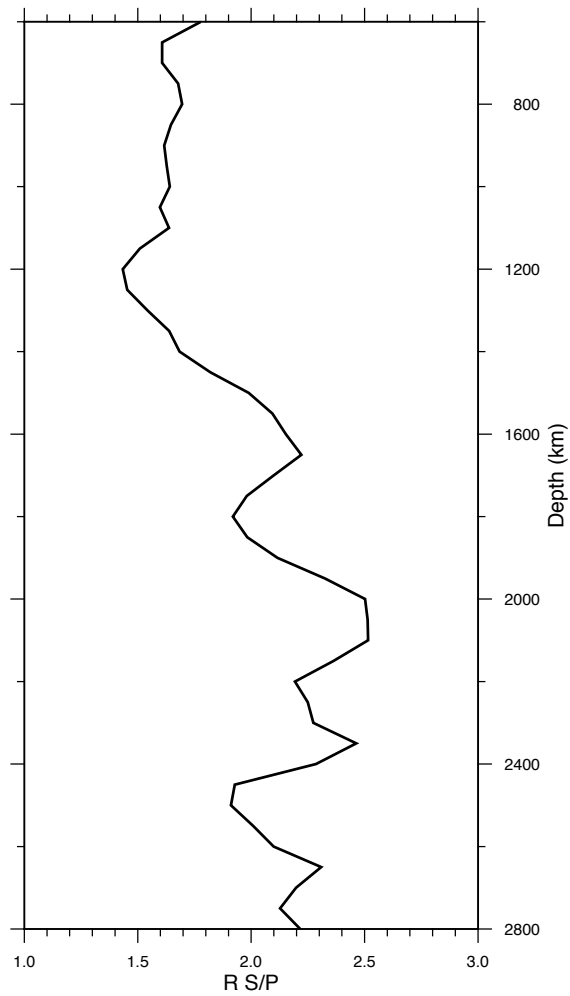
Mid-Mantle (1,000-2,200 km depth)
Reference Distributions (black)
Gaussian Fits (magenta)
in the Interval $\pm 1\sigma$ (green)
Obtained by Iterative Fitting



Supplementary Figure 11

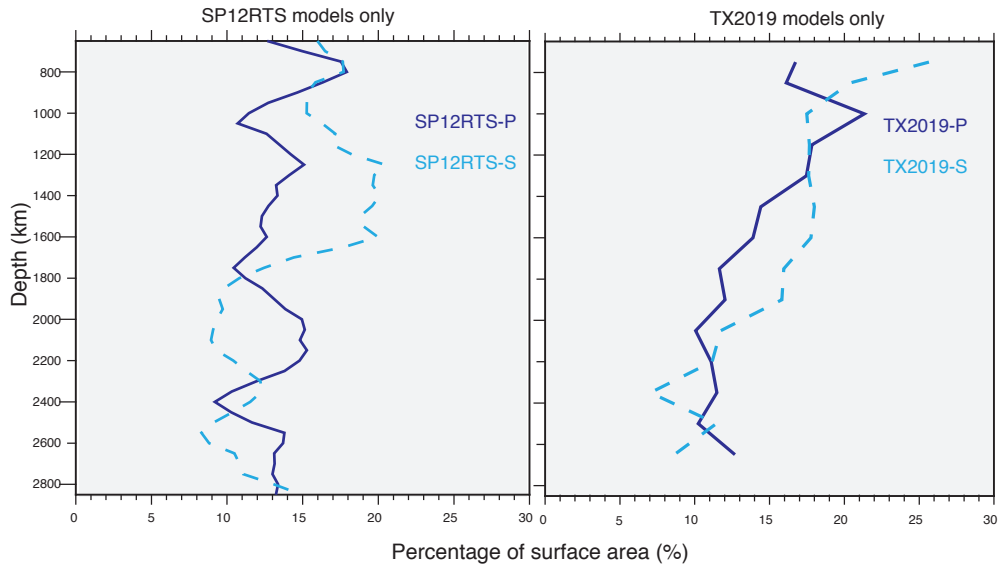


d.



Supplementary Figure 12

a. Fast anomalies ($>+1\sigma$)



b. Slow anomalies ($<-1\sigma$)

